



Title	Apodized illumination coherent diffraction microscopy for imaging non-isolated objects
Author(s)	Krishna, Khakurel Prasad
Citation	北海道大学. 博士(情報科学) 甲第12634号
Issue Date	2017-03-23
DOI	10.14943/doctoral.k12634
Doc URL	http://hdl.handle.net/2115/65681
Type	theses (doctoral)
File Information	Krishna_Prasad_Khakurel.pdf



[Instructions for use](#)

Apodized Illumination Coherent Diffraction Microscopy for Imaging Non-Isolated Objects

Doctoral Thesis

Submitted by

Krishna Prasad Khakurel



HOKKAIDO
UNIVERSITY

Graduate School of Information Science and Engineering

Hokkaido University

2017

Contents

Chapter I. Introduction.....	1
References.....	7
Chapter II. Theory.....	10
2.1 Fourier transform and its properties.....	10
2.1.1 Properties of Fourier transform.....	11
2.2 Scalar Diffraction Theory	13
2.2.1 Solution of the wave equation.....	15
2.3 Coherent Diffraction Imaging.....	17
2.3.1 Coherence	19
2.3.2 Oversampling for CDI	24
2.3.3 Phase retrieval algorithms.....	28
References.....	34
Chapter III. Introduction to Apodized illumination Coherent Diffraction Imaging	35
References.....	39
Chapter IV. Experiment with visible light.....	40
4.1 Introduction.....	40
4.2 Optical Design	41
4.3 Experimental Results and Discussions	44
4.3.1 Optical setup	44

4.3.3 Imaging of phase object.....	50
4.4 Conclusions.....	54
References.....	55
Chapter V. Generation of apodized x-ray illumination and its application to scanning and diffraction microscopy	56
5.1 Introduction.....	57
5.2 Synchrotron X-ray Source	58
5.3 X-ray Mirrors	59
5.4 Experimental setup.....	60
5.5 Design of the apodizing slit system and the apodization experiment.....	66
5.6 SXFM with apodized illumination.....	68
5.7 Coherent diffractive imaging with apodized illumination.....	71
5.8. Conclusions.....	75
References.....	77
Chapter VI. Conclusions and Future Prospects	78
Acknowledgement	79

Abstract:

Microscopy is one of the widely exploited tools in the modern scientific research. Various modalities of microscopes with different probes exist today. With the nature of the probe used, the complexity of the design and the functioning of the microscopic techniques differ. The core content of this thesis describes the development of a category of microscopic technique which performs imaging without making the use of any imaging (objective) lens. It rather reconstructs the image computationally by using iterative phase retrieval algorithms. Such microscopic or imaging technique is known in the user community as lens less imaging.

The lens less imaging method that will be discussed in this thesis is coherent diffraction imaging (CDI). The method is characterized by the formation of image by computational lens dispensing the need of physical objective (imaging) lens. Hence, coherent diffraction imaging is a technique more appropriate at shorter wavelengths where fabrication of high numerical aperture objective lens is challenging.

The successful phasing of diffraction pattern in CDI requires the satisfaction of oversampling requirement. Experimentally, this condition is satisfied by limiting the measurement of only the samples with lateral dimension smaller than that of the illumination. Such restrictions, however, precludes the imaging of wide range of important samples. This thesis introduces the development of coherent diffraction imaging method which relaxes the experimental constraint of sample isolation and images the non-isolated objects with focused illumination in a non-scanning mode. This is achieved by making use of optically generated localized illumination. This optically generated localized illumination will be referred as apodized illumination.

The design and construction of optical setup, at visible light wavelength, for the generation of apodized illumination will be discussed. Coherent diffraction imaging of extended amplitude and phase object with apodized illumination will be elaborated. The imaging technique discussed here can, in principle, provide wide field of view with resolution limited only by the wavelength of light. It also has the potential to extract the quantitative phase information from cells and tissues. The non-scanning nature of the proposed imaging method would be particularly helpful in studying the dynamics of the cellular process.

The proof-of-principle experiment at visible light is extended to x-ray wavelength. A special optical system designed for this purpose will be discussed. The optical setup comprises of two pairs of deformable mirror system. The process of generation of the apodized x-ray illumination using such optical setup will be explained. The application of the apodized illumination to scanning x-ray fluorescence microscopy (SXF) and to coherent diffraction imaging will be presented. Suppression of the background in the image of a test pattern, as a consequence of the use of apodized illumination, in SXFM will be presented. In addition, imaging of non-isolated test object by coherent diffraction will also be discussed. The preliminary results of image-quality enhancement in SXFM can be extended to biologically important specimen. Imaging of non-isolated specimen by coherent diffraction imaging can also be further developed to obtain structural and functional information of samples with biological and material importance. The method will be more advantageous for imaging extended objects by coherent diffraction imaging with x-ray free electron laser where other existing methods fall short.

Chapter I. Introduction

The extension of the horizons of fundamental knowledge across various domains of science is complemented by the introduction and advancement of the novel techniques. In the short history of modern science, wide varieties of such techniques have been developed. Among these, microscopy is one of the oldest and most exploited techniques. For a considerable period, microscopy has been used in various studies of historical importance. Had there been no advancement in such techniques, the scientific community would not have been able to build up such coherent volume of knowledge.

Optical microscopes are the oldest and the most widely used microscopes. They are ubiquitous in modern laboratories and are the workhorse of biologist. However, conventional optical microscopes cannot assist in observing the features smaller than 200 nm [1], a value limited by the wavelength of illuminating light.

To overcome the problem of resolution-limit with the optical microscope, electron microscopes have been developed and used for more than eight decades. The short De-Broglie-wavelength of the electrons can scale down the resolutions by a factor larger than 1000 compared to that of the optical microscopes. But this improvement comes with the stringent requirement in the sample preparation. The vacuum environment indispensable for the electron microscopes may not be suitable for the study of several biologically important specimens. In addition, the short penetration depth of the electron waves presents additional challenges in sample preparation and the goal of observing biological specimens in their natural state remains a feat unconquered.

For long, scientists have envisioned that, the challenges with the electron microscope

can be addressed by the exploitation of x-rays as the microscopic probe. The short wavelength of x-ray provides resolution better than that of the optical counterpart and the long penetration length overcomes the difficulties in the sample preparation with electron microscopes. In addition, predictions have also been made that the observation of the specimens in an environment analogous to its natural occurrence can be made with such x-ray microscopes [2, 3]. However, the realization of x-ray microscopes has its major difficulty in developing the perfect imaging optics, i. e. an objective lens whose performance is only limited by the phenomenon of diffraction. This conundrum can be solved with the introduction of the lens less imaging techniques such as holography and coherent diffraction imaging. This introduction will present a brief review of the later.

In 1952, David Sayre came up with a proposition to solve the phase problem for the non-crystalline materials [4]. The idea based on the sampling theory in information science states that if the diffraction intensities are sampled finer than the Nyquist frequencies, the phase problem can be solved for non-periodic objects dispensing the need of arranging the objects in the arrayed or crystalline structure. At that point in time two immediate challenges were present in order to realize Sayre's proposition. The first was the collections of the oversampled coherent diffraction patterns which was limited by the availability of the coherent light sources and second the lack of algorithms which could successfully map the phase of the oversampled diffraction pattern. The latter being a complete computational approach reconstructs the object image without the necessity of the lens. Hence the method is called a lens-less imaging method and is more suitable technique at shorter wavelength radiation where perfect imaging lens are more challenging to fabricate.

The early works in the extension of the idea of David Sayre were largely devoted in

development of the efficient computational approach to retrieve the phase from the diffraction patterns. The pioneering efforts in the development of phase retrieval techniques were made by Gerchberg and Saxton [5, 6]. Several spectacular developments in 1970's and 80's were made by Bates [7] and Fineup [8-10], following the works of Gerchberg and Saxton. By the late 1980's Fineup had already developed a reliable phase retrieval method which could be practically applied to perform the phasing of the diffraction pattern. With the advent of the third generation synchrotrons, coherent x-rays became readily available and the source limitation in realizing Sayer's proposition was resolved. Finally, in 1999 the first demonstration of imaging of a non-periodic object by a coherent diffraction imaging was made by Miao et al. [11]. Since then, this technique has gone through a revolutionary development and is one of the widely used techniques by the biologist and material scientist.

Since the demonstration of the coherent diffraction imaging, it has been applied to wide range of targets of biological and material importance such as nanoparticles, nanocrystals, cells, cell-organelles, virus, and fuel cells by using synchrotrons, soft x-ray lasers and electrons [12-29]. The method has also been demonstrated in tomographic configuration to obtain three dimensional images of the cells (cryogenic), cell organelles, and nanoparticles [30-32]. With the new bright, coherent and ultra-short pulses from the x-ray free electron lasers, imaging of live cells, various phase of cell cycle have been reported [33,34]. Recently, three dimensional imaging of one of the largest virus, Mimi virus, has been reported with x-ray laser diffraction [35]. The method has also been used in the quantitative phase mapping of nanocrystals, strain mapping in nanocrystals and in evaluation of the size distribution of nano-particles [36-38].

The computational part of the method itself has evolved to a significant extent since

its first demonstration. Different varieties of phase retrieval algorithms with improved performances have been proposed over the years. Practical method to update the object boundaries (support) in real-space has been devised [39]. The convergence of these algorithms largely depends on the noise level in the diffraction pattern. Noise tolerant phase retrieval algorithm providing high fidelity reconstructions, even in the presence of high noise levels, has been presented by A. V. Martin et al. in 2012 [40].

The light sources and instrumentation for coherent diffraction imaging have also undergone rapid development. Bright and coherent light sources are continuously evolving. High-quality focusing optics have been developed to increase the photon density and hence the attainable resolution by CDI. Detectors with single photon sensitivity are being used in many recent experiments reported. Instrumentation for multimodal microscopy including coherent diffraction imaging is being continuously developed [41].

In conventional coherent diffraction imaging method, plane wave illumination of the sample is a prerequisite for the successful reconstruction of sample-image. In recent, diffraction imaging method has also been demonstrated by exploiting the curved wavefront [42]. Such curved illumination based diffraction imaging has also been reported to provide improved convergence of the phase retrieval algorithm and can also image the extended objects.

For practical reasons, such as satisfaction of the oversampling requirements the conventional coherent diffraction imaging method can only image isolated objects. For the wider application of the method, this stood as a big challenge. In 2007, John Rodenberg et al. demonstrated, with visible light, a new variant of coherent diffraction imaging which can image extended (non-isolated) specimens [43]. This method, commonly known as Ptychography, requires the collection of multiple

diffraction patterns in a scanning mode. The method was later demonstrated with x-ray by the same group [44]. In 2008, Pierre Thibault et al. extended the method, at x-ray wavelength, to simultaneously retrieve both the object transmission function and the illumination wave without any prior information [45]. Since then, the method has been applied to wide varieties of scientifically important targets. The method has also found its application in wavefront characterization [46-50].

Imaging of extended objects at x-ray free electron lasers by methods operating in scanning mode such as Ptychography presents practical difficulties as the sample gets completely damaged precluding the possibilities of the multiple scans. In addition, such methods are also not the method of choice when the imaging of samples exhibiting faster dynamics is considered.

In 2013, Kimura et al. proposed a non-scanning coherent diffraction microscopy potential of imaging extended object [51]. The central idea of the method is the generation of the apodized illumination. By apodized illumination we mean an illumination which only has a main peak with its side lobes either eliminated or substantially suppressed. This thesis presents extension of the idea through the experimental demonstration at visible light and at x-ray wavelength.

The thesis comprises of six chapters of which chapter I is the introduction. Chapter II briefly introduces the scalar wave equation, the coherence properties of the light sources and the basics of coherent diffraction imaging technique. A quick introduction of the concept of Apodized illumination coherent diffraction imaging of extended object is presented in Chapter III. Chapter IV will be used in describing the visible light experiment on apodized illumination coherent diffraction imaging. The discussion on the generation of x-ray apodized illumination and its application to scanning x-ray fluorescence microscopy and coherent diffraction imaging will be

discussed in the chapter V. Finally, the conclusion and the future prospect will be presented in the chapter VI of the thesis.

References

- [1] E. Abbe, M. Schulze's Archive für Mikroskopische Anatomie IX, 413 (1873).
- [2] C. Jacobsen, Soft x-ray microscopy, Trends in Cell Biology **9**(2), 44-47(1999).
- [3] R. Henderson, Quart. Rev. Biophys., **28**, 171–93 (1995).
- [4] D. Sayre, Acta Cryst. 5 (6) , 843 (1952).
- [5] R. W. Gerchberg and W. O. Saxton, Optik. 34, 275 (1971).
- [6] R. W. Gerchberg and W. O. Saxton, Optik. 35, 237(1972).
- [7] R. H. T. Bates, Optik, 61, 247-262 (1982).
- [8] J. R. Fienup, Opt. Lett. 3(1), 27–29 (1978).
- [9] Fienup, J.R. Appl. Opt. 21, 2758 (1982).
- [10] Fienup, R. J. Opt. Soc. Am. A4, 118 (1987).
- [11] J. Miao et al., Nature 400, 342-344 (1999).
- [12] J. Miao et al., Phys. Rev. Lett, **95**, 085503 (2005).
- [13] Y. Takahashi et al, Nano Lett., **10**, 1922–1926 (2010).
- [14] J. M. Zuo et al., Science, **300**, 1419–1421 (2003).
- [15] I. K. Robinson et al., Phys. Rev. Lett., **87**, 195505 (2001).
- [16] G. J. Williams et al., Phys. Rev. Lett., **90**, 175501,(2003).
- [17] M. A. Pfeifer et al., Nature, **442**, 63–66 (2006).
- [18] H. Jiang et al., Phys. Rev. Lett., **100**, 038103 (2008).
- [19] J. Miao et al., Proc. Nat. Acad. Sci. USA, **100**, 110–112 (2003).
- [20] D. Shapiro et al., Proc. Nat. Acad. Sci. USA, **102**, 15343–15346 (2005).
- [21] G. J. Williams et al., Cytometry Part A, **73**, 949–957 (2008).
- [22] X. Huang et al., Phys. Rev. Lett., **103**, 198101 (2009).
- [23] J. Nelson et al., Proc. Nat. Acad. Sci., **107**, 7235–7239 (2010).
- [24] C. Song et al., Phys. Rev. Lett., **101**, 158101 (2008).

- [25] R. L. Sandberg et al., Phys. Rev. Lett. **99**, 098103 (2007).
- [26] R. L. Sandberg et al., Proc. Nat. Acad. Sci. USA, **105**, 24–27 (2008).
- [27] A. Ravasio et al., Phys. Rev. Lett., **103**, 028104 (2009).
- [28] H. N. Chapman, Nat. Phys., **2**, 839–843 (2006).
- [29] O. Kamimura et al., Appl. Phys. Lett., **92**, 024106 (2008).
- [30] J.A. Rodriguez et al., IUCrJ **2**, 575–583 (2015).
- [31] Y. Nishino et al., Phys. Rev. Lett., **102**, 018101 (2009).
- [32] M. A. Pfeifer et al., Nature, **442**, 63–66 (2006).
- [33] T. Kimura et al., Nat. Commun. **5**, 3052 (2014).
- [34] G. V. D. Schot et al., Nat. Commun. **6**, 5704 (2015).
- [35] T. Ekeberg et al., Phys. Rev. Lett., **114**, 098102 (2015).
- [36] I. Robinson, and R. Harder, Nat. Mater. **8**, 291–298 (2009).
- [37] M. C. Newton et al., Nat. Mater., **9**, 279–279 (2010).
- [38] Y. Takahashi et al, Nano Lett., **13**, 6028–32 (2013)
- [39] S. Marchesini, et al., Phys. Rev. B, **68**, 140101 (2003).
- [40] A. v. Martin et al., Opt. Express, **20**, 16650–16661 (2012).
- [41] J. Deng et al., Proc. Nat. Acad. Sci. USA, **112**, 2314–2319 (2015).
- [42] B. Abbey et al., Nat. Phys., **4**, 394–398 (2008).
- [43] J.M. Rodenburg et al., Ultramicroscopy, **107**, 227–231 (2007).
- [44] J. M. Rodenburg et al., Phys. Rev. Lett., **98**, 034801 (2007).
- [45] P. Thibault et al., Science, **321**, 379–382 (2008).
- [46] M. Dierolf et al., Nature, **467**, 436–439 (2010).
- [47] M. Holler et al., Sci Rep., **4**, 3857 (2014).
- [48] D. A. Shapiro et al., Nat. Photon. **8**, 765–769 (2014).
- [49] C. M. Kewish et al., Opt Express. **18**, 23420 (2010).

- [50] I. Zanette et al., *Sci Rep.*, **5**, 9210 (2015).
- [51] T. Kimura et al., *Opt. Express*, **21**, 9267-9276 (2013).

Chapter II. Theory

This chapter introduces the theoretical aspect of the coherent diffraction imaging. It begins with the introduction of the Fourier transform and its fundamental properties. Then a brief account of the scalar diffraction theory followed by the Fresnel and Fraunhofer approximations will be presented. The theoretical groundwork of coherent diffraction imaging will then be discussed. The basic concept of oversampling and coherence will also be presented.

2.1 Fourier transform and its properties

The employment of the Fourier theory in the development of mathematical formulation of the diffraction physics has become a common practice [1]. Hence, we will first define the continuous Fourier transform and review its basic properties. The concept of Discrete Fourier Transform will be introduced in the later part of this section.

Let us assume (x,y) and (u,v) be the variables in two arbitrary planes. The wavefields $g(x,y)$ and $G(u,v)$ in the two planes can be related by the Fourier transform as,

$$G(u,v) = F\{g(x,y)\} = \iint g(x,y) \exp[-j2\pi(f_x x + f_y y)] dx dy. \quad (2.1)$$

Here $f_x = u / \lambda z$ and $f_y = v / \lambda z$ are the frequencies at the Fourier plane. The definition of the inverse Fourier transform follows as,

$$g(x,y) = F^{-1}\{G(f_x, f_y)\} = \iint G(f_x, f_y) \exp[-j2\pi(f_x x + f_y y)] df_x df_y, \quad (2.2)$$

The operator F and F^{-1} represents Fourier transform and inverse Fourier transform respectively. Throughout this thesis the notation will be adopted to define Fourier transform and inverse Fourier transform.

2.1.1 Properties of Fourier transform

Some fundamental properties of the Fourier transform will be reviewed in this section.

- (a) Linearity: This property of Fourier transform states that the Fourier transform of a linear sum of two or more functions in the same plane is equivalent to the sum of their Fourier transforms. It can be mathematically represented as,

$$F\{ag(x, y) + bh(x, y)\} = aF\{g(x, y)\} + bF\{h(x, y)\}. \quad (2.3)$$

- (b) Similarity: The scaling of the real space frequencies will have a reciprocal effect in the Fourier plane. i.e., if the frequencies in the real space are increased, the frequencies in the Fourier plane will be decreased and vice versa.

$$F\{g(ax, by)\} = \frac{1}{|ab|} G\left(\frac{f_x}{a}, \frac{f_y}{b}\right). \quad (2.4)$$

- (c) Shift Theorem: According to the theorem, a translation in the position in the real space will result in the introduction of a linear phase shift in the Fourier plane.

$$F\{g(x - a, y - b)\} = G(f_x, f_y) \exp[-j2\pi(f_x a + f_y b)]. \quad (2.5)$$

- (d) Parseval's theorem: According to the Parseval's theorem, the integration of the square of the wave field in the real and Fourier plane are equal.

$$\iint |g(x, y)|^2 dx dy = \iint |G(f_x, f_y)|^2 df_x df_y. \quad (2.6)$$

- (e) Convolution theorem: The convolution theorem states that the Fourier transform of the product of two functions is equal to the convolution of their Fourier transforms and vice versa.

$$F\{g(x, y).h(x, y)\} = F\{g(x, y)\} * F\{h(x, y)\}. \quad (2.7)$$

- (f) Cross-correlation: According to definition of the cross-correlation,

$$F\{g(x, y)h^*(x - \varepsilon, y - \eta)\} = F\{g(x, y)\}F\{h(x, y)\}^*. \quad (2.8)$$

For the special case of $h(x, y) = g(x, y)$, the expression for cross correlation reduces to,

$$F\{g(x, y)g^*(x - \varepsilon, y - \eta)\} = |F\{g(x, y)\}|^2. \quad (2.9)$$

This is known as autocorrelation.

(g) Friedl's law: The Friedl's law states that, for a real valued function Fourier transform of the function is an even function i.e. symmetric about the origin.

$$F\{g(x, y)\} = F\{g(-x, -y)\} \quad (2.10)$$

The Fourier transform discussed so far is used to relate the continuous signals at real plane and the Fourier plane. However, in practice, measurement and storage of the signal is done only by the discrete or pixelated detectors. The mathematical tool analogous to continuous Fourier transform which suffices in the explanation of discrete signal is Discrete Fourier Transform (DFT). Here, we will define DFT in one dimension for simplicity, which can be generalized in 2D and 3D. If a function g consisting of N discrete elements is mapped into to a new function of N elements then by definition, DFT of the n th element of the function g is given as [2],

$$G_n = F(\{g\})_n = \frac{1}{\sqrt{N}} \sum_{m=0}^{N-1} g_m \exp(-2j\pi m / N), 0 \leq n \leq N-1. \quad (2.11)$$

Similarly, the inverse DFT is defined as,

$$g_n = F(\{G\})_n = \frac{1}{\sqrt{N}} \sum_{m=0}^{N-1} G_m \exp(2j\pi m / N), 0 \leq n \leq N-1. \quad (2.12)$$

All the properties discussed for the continuous Fourier transform are equally valid for the Discrete Fourier Transforms.

2.2 Scalar Diffraction Theory

Maxwell's seminal work in electromagnetics established the framework in which light can be understood as an electromagnetic wave. The work has eased the development of the mathematical formulation of the propagation of light wave. In this section we will briefly review the preliminaries required to understand the concept of scalar diffraction theory. We will setup scalar wave equation starting with the Maxwell's equation and then define the Fresnel and Fraunhofer approximation.

For a linear, isotropic medium free of charge the Maxwell's equations for electromagnetic waves can be written as,

$$\nabla \cdot \epsilon \mathbf{E} = 0 \quad (2.13 \text{ (a)})$$

$$\nabla \cdot \mu \mathbf{H} = 0 \quad (2.13 \text{ (b)})$$

$$\nabla \times \mathbf{E} = -\mu \frac{\partial \mathbf{H}}{\partial t} \quad (2.13 \text{ (c)})$$

$$\nabla \times \mathbf{H} = \epsilon \frac{\partial \mathbf{E}}{\partial t} \quad (2.13 \text{ (d)})$$

The symbols \mathbf{E} , \mathbf{H} , ϵ , and μ are used to represent electric field, magnetic field, permittivity and permeability respectively. Taking the curl of equation 2.13 (c) we get,

$$\nabla \times (\nabla \times \mathbf{E}) = -\mu \frac{\partial (\nabla \times \mathbf{H})}{\partial t} \quad (2.14)$$

Using the vector identity $\nabla \times (\nabla \times \mathbf{A}) = \nabla (\nabla \cdot \mathbf{A}) - \nabla^2 \mathbf{A}$, and the Maxwell's equations, the equation 2.14 reduces to,

$$\nabla^2 \mathbf{E} - \mu \epsilon \frac{\partial^2 \mathbf{E}}{\partial t^2} = 0. \quad (2.15)$$

With refractive index defined as, $n = \left(\frac{\epsilon}{\epsilon_0} \right)^{1/2}$ and the velocity of light, $c = \frac{1}{\sqrt{\mu_0 \epsilon_0}}$ the

equation 2.15 can be written as,

$$\nabla^2 \mathbf{E} - \frac{n^2}{c^2} \frac{\partial^2 \mathbf{E}}{\partial t^2} = 0. \quad (2.16)$$

The above equation is also satisfied by the magnetic field,

$$\nabla^2 \mathbf{H} - \frac{n^2}{c^2} \frac{\partial^2 \mathbf{H}}{\partial t^2} = 0. \quad (2.17)$$

Hence, a more general equation satisfying all the components of the electric field and the magnetic field can be written as,

$$\nabla^2 u(P,t) - \frac{n^2}{c^2} \frac{\partial^2 u(P,t)}{\partial t^2} = 0, \quad (2.18)$$

Where $u(P,t)$ is an arbitrary scalar field and the equation represents the scalar wave equation.

The expression in equation 2.18 equally represents the monochromatic and polychromatic waves. Considering a strict case of monochromatic wave the scalar field can be written as,

$$u(P,t) = A(P) \cos[2\pi\nu t - \phi(P)], \quad (2.19)$$

Where $A(P)$ and $\phi(P)$ are the amplitude and the phase of the scalar field and ν the frequency of the electromagnetic wave. Rewriting the equation 2.19 in the complex notation we obtain,

$$u(P,t) = \text{Re}\{U(P) \exp(-j2\pi\nu t)\}, \quad (2.20)$$

where $U(P) = A(P) \exp[j\phi(P)]$, is the complex function dependent on the position.

By linearity of the wave equation, the real part of the scalar field needs to satisfy the scalar wave equation and hence the wave equation can be written in the form,

$$(\nabla^2 + n^2 k^2)U = 0. \quad (2.21)$$

The equation is known as Helmholtz equation and $k = 2\pi/\lambda$ is known as the wave

number.

2.2.1 Solution of the wave equation

In order to establish the understanding of the propagation of the light and the phenomenon of scattering, it is important to find the general solution of the wave equation. For this, we rewrite the equation 2.21 as,

$$\nabla^2 U + k^2 U = -4\pi F U, \quad (2.22)$$

Where $F = \frac{1}{4\pi} k^2 [n^2 - 1]$ is called the scattering potential of the medium.

Assuming the Green's function $G(r - r')$ as solution of the equation we obtain,

$$(\nabla^2 + k^2)G(r - r') = -4\pi\delta(r - r'), \quad (2.23)$$

Physically, this means that the solution of a point scatterer object is the Green's function $G(r - r')$. Kirchhoff made a special choice of this function as

$G(r - r') = \frac{\exp[ik|r - r'|]}{|r - r'|}$. This further simplifies the interpretation of the solution of

the wave equation, according to which for a point scatterer the solution of wave equation is a spherical wave.

The concept of point scatterer as a source of the spherical wave lays the foundation of the Huygens-Fresnel theory of diffraction. According to the Huygens-Fresnel principle the wavefield at any arbitrary plane distant from the source is given by,

$$U(x, y) = \frac{z}{j\lambda} \iint U(\xi, \eta) \frac{\exp(jkr_{01})}{r_{01}^2} d\xi d\eta. \quad (2.24)$$

In the equation, $r_{01} = \sqrt{z^2 + (x - \xi)^2 + (y - \eta)^2}$ is the distance between the two points in two different planes as shown in Fig 2.1. Under paraxial approximation, the binomial expansion of r_{01} gives,

$$r_{01} = z \left[1 + \frac{1}{2} \left(\frac{x - \xi}{z} \right)^2 + \frac{1}{2} \left(\frac{y - \eta}{z} \right)^2 \right] \quad (2.25)$$

Using equation 2.25 in equation 2.24, we get

$$U(x, y) = \frac{e^{jkz}}{j\lambda z} \iint U(\xi, \eta) \exp \left\{ j \frac{k}{2z} [(x - \xi)^2 + (y - \eta)^2] \right\} d\xi d\eta, \quad (2.26)$$

Expanding the square terms inside the integral,

$$U(x, y) = \frac{e^{jkz}}{j\lambda z} e^{j \frac{k}{2z} (x^2 + y^2)} \iint U(\xi, \eta) e^{j \frac{k}{2z} (\xi^2 + \eta^2)} e^{-j \frac{2\pi}{\lambda z} (x\xi + y\eta)} d\xi d\eta, \quad (2.27)$$

For Fresnel approximation, i.e. when the distance between the two planes is relatively small, the quadratic phase factor inside the integral cannot be neglected. The expression in equation is the mathematical representation for Fresnel diffraction of a complex field. The term in the integral is the Fourier transform of the complex field scaled with a quadratic phase factor. Mathematically,

$$U(x, y) = \frac{e^{jkz}}{j\lambda z} e^{j \frac{k}{2z} (x^2 + y^2)} F \left\{ U(\xi, \eta) e^{j \frac{k}{2z} (\xi^2 + \eta^2)} \right\}. \quad (2.28)$$

$$\text{For large value of } z \text{ i.e., } z \gg \frac{k(\xi^2 + \eta^2)}{2} \quad (2.29)$$

the quadratic factor in the equation 2.27 can be neglected and hence the equation can be written as,

$$U(x, y) = \frac{e^{jkz}}{j\lambda z} e^{j \frac{k}{2z} (x^2 + y^2)} \iint U(\xi, \eta) e^{-j \frac{2\pi}{\lambda z} (x\xi + y\eta)} d\xi d\eta. \quad (2.30)$$

The approximation made is known as Fraunhofer approximation. The expression in equation represents the mathematical definition for the Fraunhofer diffraction of a complex field. Unlike for Fresnel diffraction, now the terms inside the integral reduces to a simple Fourier transform of the complex field.

$$U(x, y) = \frac{e^{jkz}}{j\lambda z} e^{j\frac{k}{2z}(x^2+y^2)} F\{U(\xi, \eta)\}. \quad (2.31)$$

Equation 2.29 also gives the condition needed to be satisfied in order to obtain

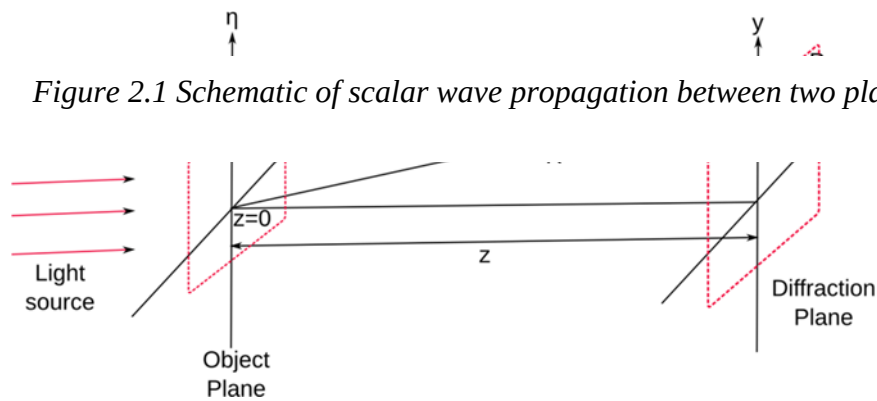


Figure 2.1 Schematic of scalar wave propagation between two planes

Fraunhofer diffraction in coherent diffraction imaging. It can be written in more general form as,

$$z \gg \frac{2a^2}{\lambda}. \quad (2.32)$$

In the equation, a is the dimension of the object. At optical wavelength, the distance z for satisfying the Fraunhofer approximation can be significantly large. The problem can be resolved by exploiting the Fourier transforming property of lens, a discussion of which will be made in chapter IV of this thesis.

2.3 Coherent Diffraction Imaging

Coherent diffraction imaging (CDI) is a lens less imaging technique. Here, a coherent or partially coherent light source illuminates an object. The scattered intensity at the Far-field (a distance that satisfies the Fraunhofer approximation i.e. equation 2.32) is

collected by a pixelated detector. This scattered amplitude is then phased by using the phase retrieval algorithm and finally the image of the scatterer is reconstructed. A schematic of the coherent diffraction imaging is shown in Fig 2.2.

The success of this technique largely depends on the availability of the coherent sources, satisfaction of the sampling requirements and the convergence of the phase retrieval algorithm. In this section, we will briefly overview these prerequisite for realizing a successful coherent diffraction imaging experiments.

The illuminating source needs to satisfy the coherence requirement for the designed experiment.

At optical wavelength, this condition is easily satisfied as coherent sources such as laser are readily available. At synchrotrons, coherent x-ray illumination is generated by selecting a fraction of the light source with a pinhole or slit. The advent of new light sources such as x-ray free electron lasers, tabletop x-ray sources increases the availability of coherent x-ray sources.

The sample is usually mounted on a transparent substrate such that the requirement of isolation of sample is satisfied. The position of the detector is determined such that the Fraunhofer approximation given in equation 2.32, oversampling requirement is satisfied and also the targeted resolution is achieved. The numerical aperture of the detector determines the resolution of the imaging system for the particular wavelength used for the sample illumination.

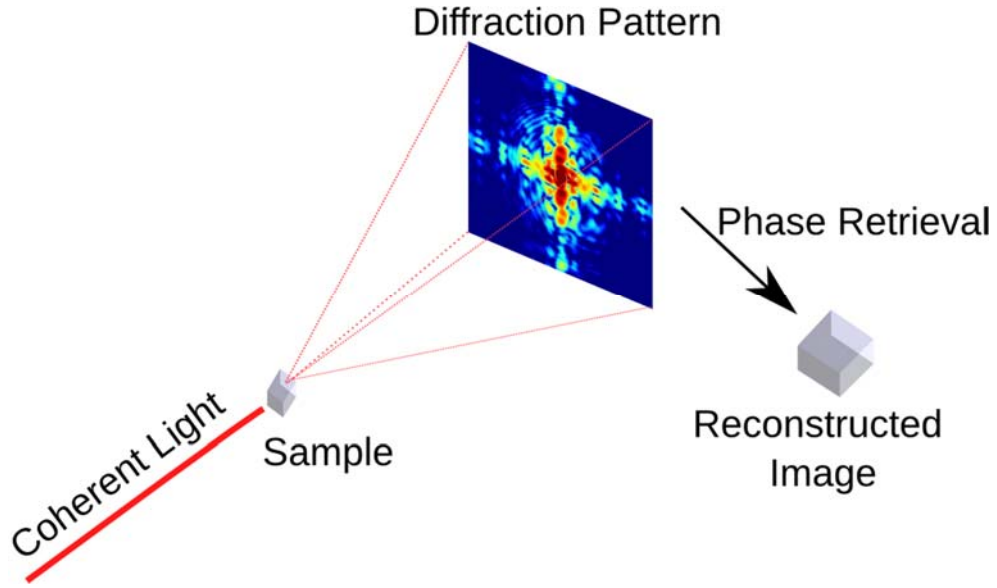


Fig. 2.2 Schematic representation of coherent diffraction imaging.

The available detector technologies can only measure the modulus square of the electric field and hence the phase of the scattered wave field remains undetermined. Appropriate phase retrieval methods must be employed in order to determine the phase. An elaborated discussion on the phase retrieval algorithms will be discussed in the later part of this section.

2.3.1 Coherence

Coherence, laser like property of light, is the measure of the correlation of wavefronts in space and time. Coherence of a light source can be intuitively explained with the aid of the optical phenomenon of interference. Let us consider two wavefronts $E_1 e^{i\phi_1}$ and $E_2 e^{i\phi_2}$ generated from the source between which a degree of correlation is to be established. Then by the superposition principle, the intensity of the superposed wave is given by,

$$\begin{aligned}
 I &= |E_1|^2 + |E_2|^2 + (E_1 E_2 e^{-i(\phi_1 - \phi_2)} + E_1 E_2 e^{i(\phi_1 - \phi_2)}) \\
 &= |E_1|^2 + |E_2|^2 + 2E_1 E_2 \cos(\phi_1 - \phi_2) \\
 &= |E_1|^2 + |E_2|^2 + 2E_1 E_2 \cos(\delta\phi),
 \end{aligned} \tag{2.33}$$

where $\delta\phi$ is the phase difference between the superimposing wavefronts. Based on the intensity modulation term in the equation the source can be classified as coherent or incoherent. Perfect coherence and incoherence are idealized concepts. However, if the intensity modulation term $\cos(\delta\phi)$ is non-zero, the two wavefronts are said to possess finite correlation and the source is said to be coherent. Sources such as laser fall under this category. On the contrary, if the phase difference between the wavefronts $\delta\phi$ vary randomly, then the intensity modulation term $\cos(\delta\phi)$ is zero which concludes that the wavefronts are perfectly uncorrelated and the sources are said to be incoherent. The common light sources such as sunlight, fluorescent lamp represents the incoherent sources. The light sources such as LED, synchrotron radiation which fall in between these two extremes of coherence are usually termed as partially coherent sources. The coherence properties of light can be studied under two broad categories viz. longitudinal coherence and transverse coherence [3].

Longitudinal coherence:

The coherence property of light along the direction of propagation is called longitudinal coherence or temporal coherence. It provides the measure of the correlation of wavefronts in time. Common amplitude division interferometers such as Michelson interferometer or Mach Zehnder interferometer can be employed to test the longitudinal coherence of the light sources. Let us consider two wavefronts of wavelengths λ and $\lambda + \Delta\lambda$ propagating along the same direction starting from the same point as shown in Fig 2.3 (a). The wavefronts are in and out of phase periodically. Let, $2\varepsilon_l$ be the distance in which these in-phase wavefronts completes a phase-out phase-in cycle. We assume that the wavefronts have N and $N-1$ oscillations within this period. Then, we can comfortably write $N\lambda = (N-1)(\lambda + \Delta\lambda)$.

Solving the equation we get, $N = \frac{\lambda}{\Delta\lambda}$. Hence the coherence length can be represented

as,

$$\varepsilon_l = \frac{\lambda^2}{2\Delta\lambda}. \quad (2.34)$$

Physically, the longitudinal coherence length is inversely proportional to the bandwidth of the source i.e. for an ideal monochromatic source the longitudinal coherence length is infinity. For synchrotron x-rays, at wavelength

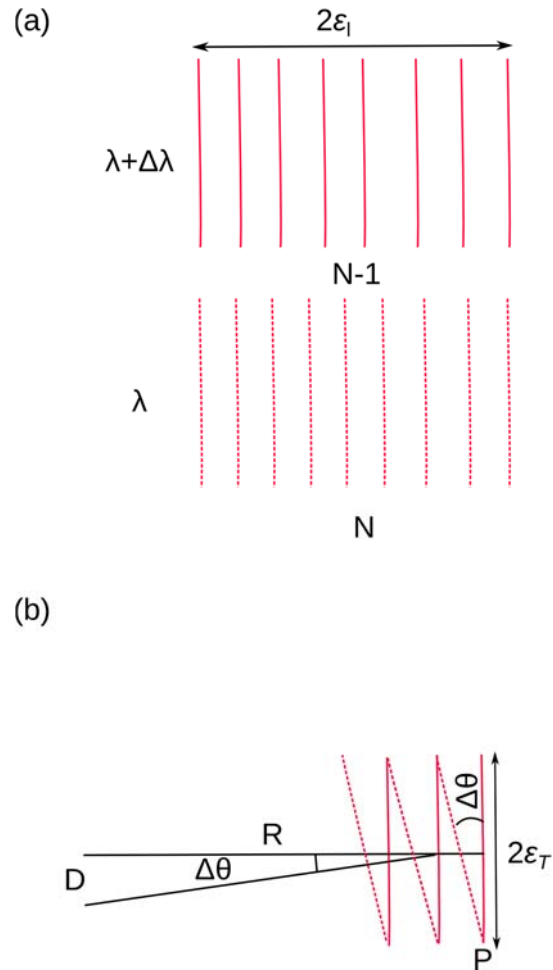


Figure 2.3 Illustrations to define the coherence of light sources (a) Longitudinal coherence (b) Transverse coherence

of 0.1 nm if the monochromaticity, $\frac{\Delta\lambda}{\lambda}$, is 10^{-6} , the coherence length, by the equation 2.34 is about 50 micron.

Transverse coherence:

The coherence property of light source along the direction perpendicular to the propagation vector is called transverse coherence and is also known as spatial coherence. Let us consider an extended source of width D as shown in Fig.2.3. The wave fronts propagating from the two end of the sources with an angular separation of $\Delta\theta$ are completely in phase at point P. The distance at which these two wave front are again in phase is assumed to be $2\varepsilon_T$. Then by geometry, $2\varepsilon_T\Delta\theta = \lambda$. Relating the angular separation with the source size and the distance of observation, R, we get

$$\varepsilon_T = \frac{\lambda}{2} \left(\frac{R}{D} \right) \quad (2.35)$$

Hence, the transverse coherence of the light source depends on the source size and the distance of observation. For an ideal point source, the transverse coherence is infinitely large and provides fringes of high visibility. In practice, such point source does not exist and we have finite coherence length. In other setup, if we increase the source distance then also the coherence length can be improved, a concept that resonates with the Van Cittert-Zernike theorem [4].

As the name implies, coherence of light source is an essentials for the coherent diffraction imaging. Illumination of the sample by coherent light source ensures that the scattered light interferes to form a speckle pattern where the information of scatterer is well preserved. On the other hand, illumination of sample by incoherent light source rules out the possibility of interference of the scattered light and what is measured in the ensemble average of the scattered intensities. This also averages out the information of the sample in the intensity distribution. Additionally, retrieval of the information from such averaged intensity distribution adds huge challenge.

2.3.2 Oversampling for CDI

The concept of oversampling has been long surveyed in the field of signal processing. However, the importance of oversampling in the phase retrieval has been identified only in early 1950's by David Sayre. In the attempt to address the phase problem of non-periodic objects, Sayre presented the idea that, if the diffraction intensities sampled finer than the Bragg peaks in the diffraction pattern can be measured, the phase problem could be solved. Bates, later, extended the idea and suggested that if the oversampling is greater than a factor of two, the phase problem can be uniquely solved [5]. This can be equivalently interpreted that an oversampling of two in each dimension is required to solve the phase. In 1998, Miao et al. presented that an oversampling of two in each dimension would not be necessary to solve the phase problem by demonstrating the numerical simulation for the two dimension and three dimension objects [6]. In addition, this work also introduced a new approach in defining the oversampling, as a ratio of the total number of the discrete units to the no of discrete units consisting of electron density (object intensity). Mathematically,

$$\sigma = \frac{\text{Total no. of pixels}}{\text{no. of pixels with electron density}} \quad (2.36)$$

According to the article, the factor $\sigma \geq 2$ is sufficient to solve the phase problem uniquely. However, a larger value of oversampling, ensures the availability of large no of equations compared to the unknowns variables, which eases the unique solution of the phase problem.

In the experiments, oversampling requirement is satisfied by designing the experimental geometry. Here, we will derive the mathematical formula that defines the degree of oversampling for any experimental geometry.

The discretization steps in the real space Δx and reciprocal space Δq , is related by DFT as [7],

$$\Delta x \Delta q = \frac{2\pi}{N} \quad (2.37)$$

The smallest unit in the reciprocal space Δq can be written as,

$$\Delta q = \frac{2\pi}{\lambda L} \delta \quad (2.38)$$

Inputting the equation 2.38 in the equation 2.37 we get,

$$\Delta x = \frac{\lambda L}{N\delta} \quad (2.39)$$

If we define the dimension of the object as a , then by oversampling condition we have,

$$\sigma = \frac{N\Delta x}{a} \geq 2 \quad (2.40)$$

Where σ is the oversampling ratio. Replacing the definition of Δx we get,

$$\sigma = \frac{\lambda L}{\delta a} \geq 2 \quad (2.41)$$

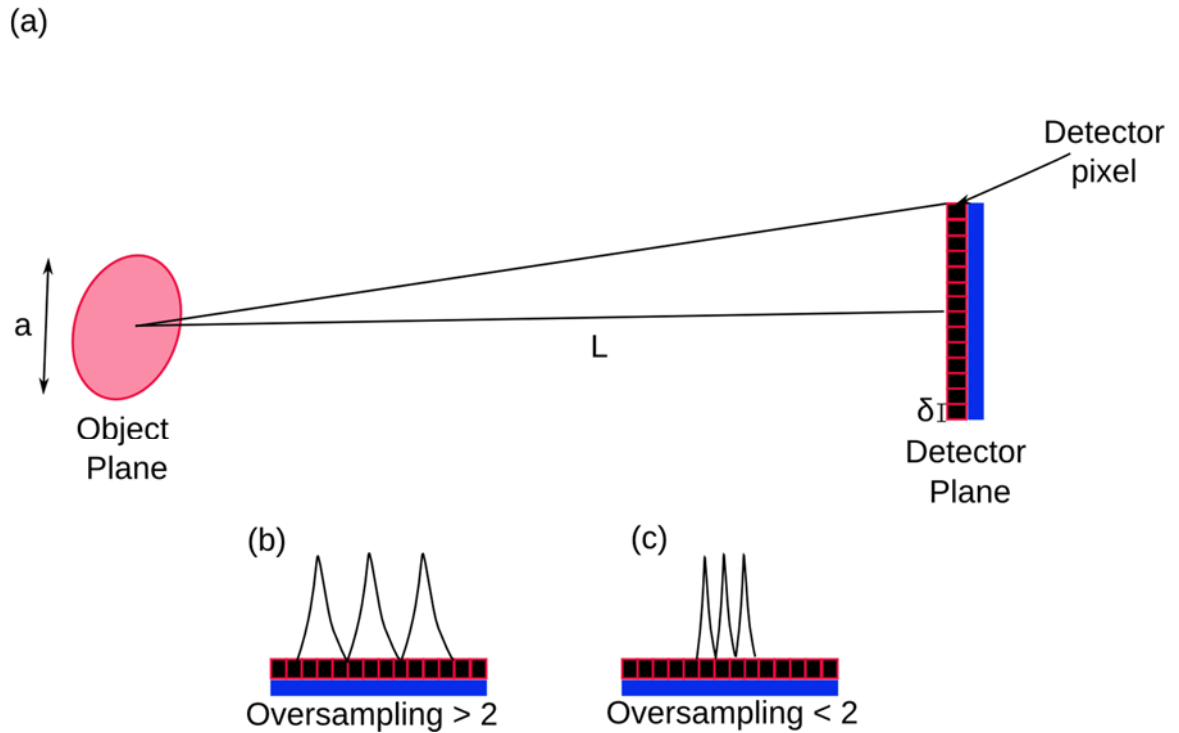


Figure 2.4 Schematic representation of Oversampling (a) the geometry of coherent diffraction imaging (b) Signals on detector with oversampling greater than 2 (c) signals with oversampling less than 2

Hence, given that the wavelength, sample-detector distance, detector pixel size and sample dimensions are known, the oversampling ratio for any experimental geometry can be determined. A schematic of the oversampling in coherent diffraction imaging is shown in Fig 2.4. The signal with oversampling greater than 2 is shown in Fig 2.4 (b) and that with smaller than 2 is shown in Fig 2.4 (c).

In the process of deriving the relation for oversampling ratio, we have also derived an important parameter ΔX i.e. the real space pixel size. This parameter provides the

estimation of the resolution for any imaging system based on coherent diffraction imaging.

The oversampling ratio can also be estimated from the speckle size in the reciprocal space provided that the dimensions of the detector pixel are known. Simplifying the statement, an oversampling ratio of 10 along one dimension indicated that the speckle is extended over 10 pixels of the detector in the reciprocal space along the corresponding direction. Here, we use a simulated coherent diffraction pattern to clarify the concept. In the Fig 2.5 (a), the central part of a simulated diffraction pattern from a gold nano cube is presented. In the diffraction pattern the speckles are clearly

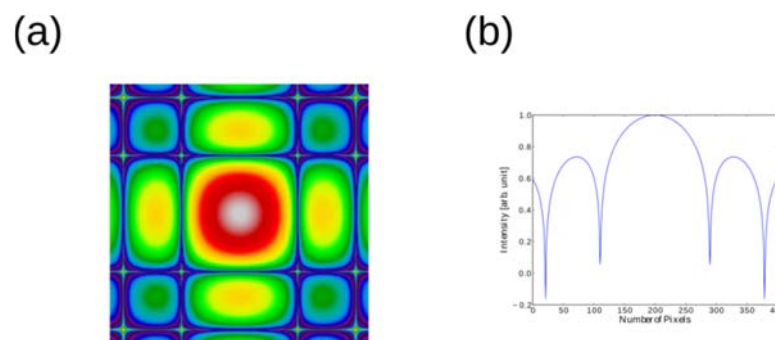


Figure 2.5 (a) simulated coherent diffraction pattern. (b) the line plot along the horizontal direction through the center of the diffraction pattern

apparent. A line plot along the horizontal direction through the center is shown in the Fig 2.5 (b). From the line plot, it becomes obvious that the speckle extends to 89 pixels of the detector along that direction which suggests that the oversampling ratio was 89.

2.3.3 Phase retrieval algorithms

Phase retrieval algorithms form an important part of the coherent diffraction imaging. So far we have dealt with the measures to collect the coherent diffraction patterns. From here onwards, a comprehensive survey of phase retrieval process will be considered.

Phase problem is well known in physics. The problem has been resolved in crystallography by using various direct and indirect methods [8]. For non-periodic objects, the interest in solving the phase problem has arose with the proposition made by David Sayre. Gerchberg and Saxton then laid the foundational work of the constructing an iterative method to retrieve the phase [9]. The iterative algorithm, devised by them is characterized by the propagation between the Fourier and the image plane. This means that intensity distribution at two different planes was required to be measured. The difficulty of measurement of two intensities didn't prove the method to be practical at the short wavelengths. The algorithm was later modified by Fineup and a more practical algorithm was presented in which intensity measurement at a single plane would suffice the retrieval of the phase [10]. The first generation of such algorithm was termed Error-Reduction algorithm. The slow convergence of the Error-Reduction algorithm forced to the development of new algorithms. In 1987, Fineup came up with an algorithm employing a feedback mechanism. The algorithm ensured fast and reliable convergence to unique solution. This method is widely known as Hybrid Input output algorithm (HIO). In the process of development of phase retrieval algorithm several other varieties of feedback mechanism have been proposed over the years. Some of the methods such as relaxed average alternative reflection averaging are intensively used in coherent diffraction imaging [11].

The architecture of the entire Fineup-type algorithm shares certain degree of similarity. They deal with the propagation of a random initial guess to and fro in the object plane and the Fourier plane. The propagation process is subjected to constraint in each plane in order to guide the algorithm to an unique solution. The primary constraint in the real space is known as support constraint and that in the Fourier plane is known as the modulus constraint. Some of these algorithms also use positivity constraint in the real space. The process of the propagation between two

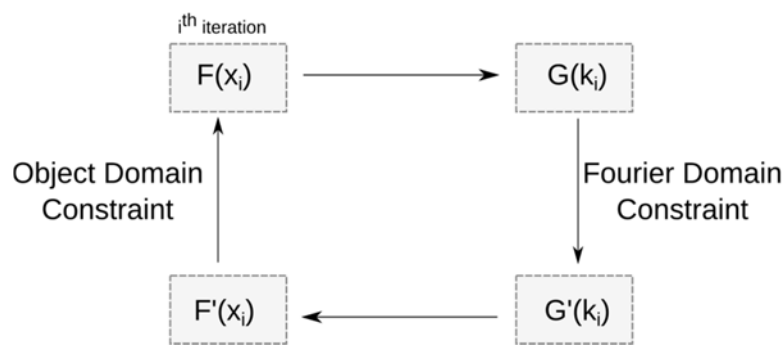


Figure 1.6 Schematic representation of the iterative phase retrieval algorithm

planes and subjection of constraints is continued until a stable unique solution is obtained.

In the earlier versions of Fineup-type algorithms, the determination of the support constraint was done from the estimate of the autocorrelation function obtained by inverse Fourier transformation of the measured diffraction intensity and was held constant for the entire iterations in one run of the algorithm. This limited the optimization of support constraint based on hit and trial method, which was very

inefficient. Additionally, in real experiments at shorter wavelength, the near center diffraction intensities are not measured which adds further uncertainties in the support estimation from the autocorrelation. In 2003, Stefano Marscheni et al. came up with a method to dynamically upgrade the support during the iterations. This method provided an efficient approach to optimize the support constraint and is now adopted by wide users in coherent diffraction imaging community [12]. The method is popular in the community as shrink-wrap hybrid input output algorithm. We will further discuss the basic iterative Fineup-type algorithm and limit our self to the shrink-wrap HIO which will be sufficient to follow the discussions in the experimental section.

Error reduction algorithm

The error-reduction algorithm is the simplest form of the Fineup-type algorithm introduced to map the phase to the diffraction pattern. The i^{th} iteration of the algorithm is shown schematically in Fig 2.6. Similar to the other variants of the Fineup-type algorithm, it begins with an initial guess in the real space, $g(x)$. The initial guess is propagated to the reciprocal space using the Fourier transform relation. The function, $G(k)$ in the reciprocal space is subjected to the modulus constraint. The new updated function, $G'(k)$ is inverse Fourier transformed where it is subjected to support and positivity constraint. The variants of the Fienup-type algorithms differ in this support constraint. The n^{th} iteration of the Fineup-type phase retrieval algorithm is represented in the form of the following equations.

$$G_n(k) = F(g_n(x)) \quad (2.42 \text{ (a)})$$

$$G'_n(k) = \text{Mod}(G_n(k)) \quad (2.42 \text{ (b)})$$

$$g_{n+1}(x) = F^{-1}(G'_n(k)) \quad (2.42 \text{ (c)})$$

$$g'_{n+1}(x) = \text{Sup}(g_{n+1}(x)) \quad (2.42 \text{ (d)})$$

In the above equations, *Mod* refers to the modulus constraint and *Sup* refers to the support constraint. The positivity constraint in the real space will be defined with support constraint in this thesis.

The Modulus constraint i. e. *Mod* in the above equation is defined as follows,

$$G'_n(k) = \begin{cases} \frac{\sqrt{I(k)_{\text{measured}}}}{|G_n(k)|} G_n(k) & \text{if } k \notin D \\ G_n(k) & \text{if } k \in D \end{cases} \quad (2.43)$$

Where D is the region in the diffraction pattern where the intensity is not measured (the region of the beam stop).

The support constraint which is the primary difference between the Error-reduction algorithm and other variants of Fineup-type algorithm is defined as,

$$g'_{n+1}(x) = \begin{cases} 0 & \text{if } x \notin S \text{ and } g_{n+1}(x) < 0 \\ g_{n+1}(x) & \text{if } x \in S \text{ and } g_{n+1}(x) \geq 0 \end{cases} \quad (2.44)$$

This equation explains that in every iteration of Error-reduction algorithm, the value outside the support region is reduced to zero and that within the support the function is retained. S in the equation represents the support region.

Shrink-wrap Hybrid Input Output

The more advanced version of the phase retrieval algorithm is HIO algorithm. The overall logical flow of the algorithm is analogous to the error reduction algorithm apart from the application of the support constraint. Unlike in error reduction algorithm, the region outside the support is gradually reduced to zero by introducing a feedback parameter. The support constraint used in HIO can be defined as,

$$g'_{n+1}(x) = \begin{cases} g_{n+1}(x) - \beta g_n(x) & \text{if } x \notin S \\ g_{n+1}(x) & \text{if } x \in S \end{cases} \quad (2.45)$$

Here, β is the feedback parameter and its value is chosen in between 0.5 and 1.

In the support constraint, the appropriate method to optimize the support size is crucial in the successful reconstruction of the complex wave field. A practical way in this approach is suggested in the shrink-wrap algorithm. Here, the initial guess for the support is gradually updated in regular steps. In the original idea presented the initial support is determined from the autocorrelation which is gradually updated by taking a threshold maximum of the reconstructed amplitude and convoluting with a Gaussian of width of 3 pixels. The threshold and the width are the factor to be optimized during the reconstruction process. This process is repeated in the step of a few iterations which assists in getting the support size and shape closer to that of the object. The graphical representation of the shrink-wrap HIO algorithm is shown in the Fig 2.7.

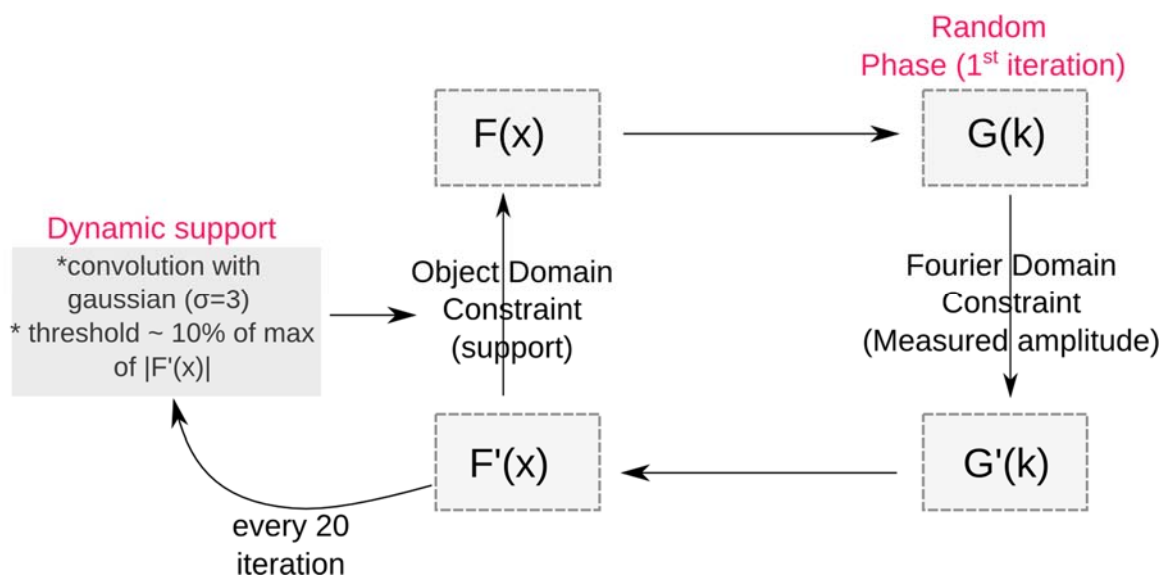


Figure 2.7 A schematic of the Shrink-wrap algorithm which using dynamic support constraint in real space.

References

- [1] J. Goodman, Introduction to Fourier Optics (Roberts and Company, 2004).
- [2] D. Voelz, Computational Fourier Optics (SPIE Press, 2011).
- [3] J. A. Nielsen and D. McMorrow, Elements of Modern X-ray Physics (John Wiley & Sons, Ltd, 2011).
- [4] M. Born and E. Wolf, Principles of Optics (Cambridge University Press, 1999).
- [5] R. H. T. Bates, Optik, 61, 247-262 (1982).
- [6] J. Miao et al., Opt. Soc. Am. A, **15**, (1998).
- [7] P. Thibault et al., Am. J. Phys. **75**, 827 (2007)
- [8] D. E. Sands, Introduction to Crystallography (Dover Publications Inc., 1969).
- [9] R. W. Gerchberg and W. O. Saxton, Optik. 35, 237(1972).
- [10] Fienup, J.R. Appl. Opt. 21, 2758 (1982).
- [11] D. R. Luke, Inverse Problems **21**, 37-50 (2005).
- [12] S. Marchesini, et al., Phys. Rev. B, **68**, 140101 (2003).

Chapter III. Introduction to Apodized illumination Coherent

Diffraction Imaging

In the previous chapter we had defined some of the prerequisites for the realization of successful coherent diffraction imaging. In the process, we dealt with the oversampling requirement in coherent diffraction experiment. In practice, the oversampling requirement is satisfied by measuring only the isolated samples. This precludes the imaging of wide varieties of important targets whose lateral dimensions are larger than that of the illumination. Methods which can resolve this conundrum by using a divergent illumination or by operating the diffraction imaging in a scanning

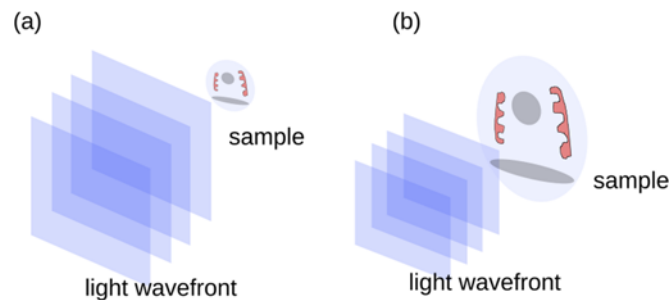


Figure 3.1 Graphical representation of illumination of (a) isolated object (b) extended object

mode has been discussed in the introduction of this thesis. More recently, Kimura et al. have proposed a non-scanning coherent diffraction imaging method which can image extended object employing focused illumination [1]. The article introduces a method to generate spatially localized illumination by using a special optical setup. The localized illumination does the lateral sectioning of the extended object and hence produces an isolated exit wave. The concept of isolated object and extended object has been shown graphically in the Fig 3.1 (a) and (b) respectively.

The use of focusing optics in spectro-microscopic technique across various wavelengths in the electromagnetic spectrum is a common practice. Since the wave

field at the focal plane of such devices is the Fourier transform of the wavefield at the exit pupil, the intensity distribution at the focal plane is defined by the geometrical shape of the focusing devices. For instance, a plane wave focused by a spherical lens has the intensity distribution comprising of a central disc surrounded by a concentric rings. Hence, the focused intensity distributions are extended and consist of a strong main lobe accompanied by the side lobes. These side lobes deteriorate the quality of the measurements in the spectro-microscopic techniques. The mechanism of getting rid of such side lobes is called apodization and thus generated illumination in which the side lobes are either completely eliminated or substantially suppressed is called apodized illumination. Generation of such apodized illumination is the central concept behind the imaging of non-isolated object with coherent diffraction imaging in a non-scanning mode. The overall concept behind the apodized illumination coherent diffraction imaging of non-isolated object is explained by means of a numerical simulation [2].

For the numerical simulation, we employed the experimental setup shown in Fig 4.1 of Chapter IV. A detailed explanation of the optical setup is summarized in the experimental setup section of the chapter. The optical setup is characterized by the presence of the intermediate plane where an apodizing slit is placed. The intensity distribution at the sample plane can be controlled by varying the aperture size of the apodizing slit. To make the discussion consistent throughout the thesis (i.e. for both the experiments discussed in this thesis), we call the plane of apodizing slit as the first focal plane and the sample plane as the second focal plane.

The outcome of the numerical simulations is summarized in the Fig 3.2. The intensity distribution at the intermediate plane i.e. the 1st focal plane without and with apodizing slit is shown in Fig.3.2 (a) and (b) respectively. While the intensity

distribution at the sample plane without and with apodizing slit is shown in the Fig. 3.2 (c) and (d) respectively. It is apparent from the figure that the side lobes present in the intensity distribution at the sample plane is substantially reduced.

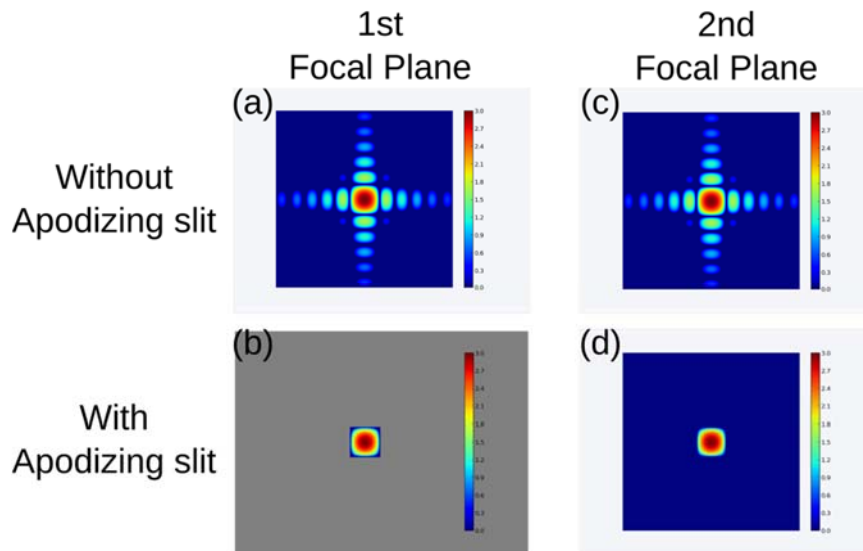


Figure 3.2 Intensity distribution at the plane of apodizing slit (a) without optimized slit aperture (b) with optimized slit aperture. Intensity distribution at the sample plane (c) without optimized slit aperture (d) with optimized slit aperture

The isolated illumination generated at the sample plane is used to perform a numerical simulation to study the feasibility of the coherent diffraction imaging of a test pattern. The test pattern is shown in the Fig 3.3 (a). The pink dotted line shown in the figure represents the region of the sample illuminated by the apodized illumination shown in Fig 3.2 (d). Fig. 3.3 (b) shows the exit wave. The figure distinctly displays that the exit wave is spatially localized. The diffraction pattern from the exit wave is shown in the Fig 3.3 (c). The image reconstruction from the diffraction pattern was performed by using shrink-wrap HIO algorithm. Fig. 3.3 (d) shows the reconstructed image after 1000 iterations. The reconstructed amplitude shows good agreement with the exit wave.

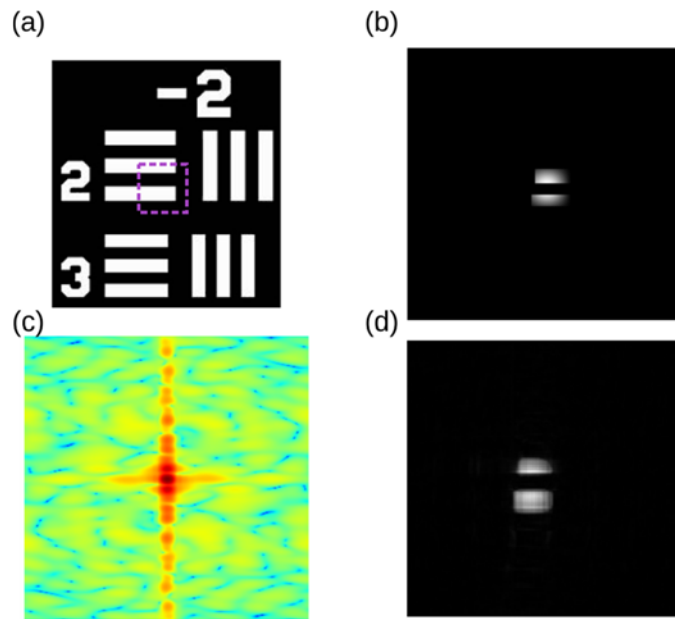


Figure 3.3 (a) Binary test pattern used as extended object for the simulation (b) the exit wave obtained by multiplying (a) with Fig. (d). the diffraction pattern obtained from (b). Reconstructed image.

To summarize, we have made an introduction to the concept of the apodized illumination and by numerical simulations understood the exploitation of such apodized illumination in the imaging of extended objects by coherent diffraction imaging.

References

- [1] T. Kimura et al., Opt. Express, **21**, 9267-9276 (2013).
- [2] K. P. Khakurel et al., Hokkaido University, School of Information Science & Technology Symposium for Young Researchers, Nov 2013.

Chapter IV. Experiment with visible light

4.1 Introduction

Many objects of biological interest such as cells and tissues are transparent in their natural state at the optical wavelengths. Despite being widely exploited tools in life sciences, common absorption-contrast optical microscopes cannot display natural contrast of these transparent specimens in the in-focus image plane. Early solutions provided to the problem by Zernike's phase contrast microscopy [1,2] and differential interference contrast (DIC) microscopy [3] can transform the phase modulation of the sample into the intensity variations. These methods, however, have difficulty providing phase information quantitatively: Zernike's phase contrast microscopy is known to suffer from characteristic halo artifacts; and DIC can only provide the gradient of the phase and the image contrast is usually low.

A broad variety of interferometric methods [4–6] have been used for the quantitative phase shift measurement of biological specimens. Precise phase determination in interferometric methods, however, usually requires measurement of multiple interferograms, which is not suitable for imaging of fast cellular dynamics, and also sensitive to environmental vibrations.

Non-interferometric quantitative phase imaging methods also often demand multiple wavefield intensity patterns. The transport of intensity equation needs the intensities at multiple planes [7]. Coherent diffraction imaging (CDI) is a quantitative phase imaging method [8, 9] and has been used for high-contrast bio-imaging in the X-ray regime [10-14]. Conventional CDI, however, can practically image isolated objects only. Ptychography, a scanning coherent imaging method, can be applied to extended objects and thus broadened the applicability of CDI [15-22].

To observe fast cellular dynamics, however, quantitative phase imaging from a single wavefield intensity pattern is preferred. In the present study, we employ recently proposed “non-scanning” apodized-illumination CDI to image non-isolated objects [23]. The use of focusing optics can also make CDI measurement efficient [24-27]. In the process of development of apodized-illumination CDI, we first demonstrate the imaging of extended objects by using an optical laser. We also show that the methods are useful in imaging of transparent phase objects at the optical wavelengths.

4.2 Optical Design

The generation of isolated illumination for imaging of extended objects is the central idea of apodized-illumination CDI. Hence, we have designed an optical configuration to construct a spatially-confined constant-phase illumination. Before discussing the entire optical configuration, we briefly discuss the capability of lenses to generate a constant-phase main lobe at its back focal plane with a specific optical configuration.

The magnitude of the wavefield at the back focal plane of a lens is the Fourier transform of the wavefield placed either in front of the lens or immediately behind the lens [28]. The associated phase factor of the wavefield depends on the position of the input plane relative to the lens. Here we will first establish lens as a Fourier transformer and then will derive the expression for the generation of constant-phase focused illumination with the lens.

A lens of focal length f , introduces a phase curvature of $e^{-j\frac{k}{2f}(\xi^2+\eta^2)}$. If the input field is placed immediately in front of the lens, the wavefield at the focal plane of the lens, using Fresnel approximation defined in the equation 2.27, is given by,

$$\begin{aligned}
U(x, y) &= \frac{e^{jkz}}{j\lambda z} e^{j\frac{k}{2z}(x^2+y^2)} F \left\{ \left[U(\xi, \eta) e^{-j\frac{k}{2f}(\xi^2+\eta^2)} \right] e^{j\frac{k}{2f}(\xi^2+\eta^2)} \right\} \\
&= \frac{e^{jkz}}{j\lambda z} e^{j\frac{k}{2z}(x^2+y^2)} F \{ [U(\xi, \eta)] \}
\end{aligned} \tag{4.1}$$

Hence, at the focal plane of the lens we get the Fourier transform of the input field. However, the phase quadrature associated with the Fourier transform of the input field is not desired for the coherent diffraction imaging which requires illumination of the sample with a plane wave. So, we now derive the case in which a plane wave can be realized at the focal plane of the lens.

Let the input wavefield be placed at a distance d in front of a lens with a pupil function P . The wavefield at the back focal plane of the lens with a focal length f is given by,

$$U(x, y) = \frac{e^{jkz \left[j\frac{k}{2f} \left(1 - \frac{d}{f} \right) (x^2 + y^2) \right]}}{j\lambda z} \times \iint U(\xi, \eta) P \left(\xi + \frac{d}{f} x, \eta + \frac{d}{f} y \right) e^{-j\frac{2\pi}{\lambda z} (x\xi + y\eta)} d\xi d\eta, \tag{4.2}$$

Provided that the pupil of the lens projected on the input plane is large compared to the dimensions of the input object, we can neglect the effect of the pupil function.

In the cases when the quadratic phase factor in equation 4.2 should be avoided, the input is placed at the front focal plane of the lens. In such case, i.e. when $d=f$, the wavefield at the back focal plane of the lens is given by,

$$U(x, y) = \frac{1}{j\lambda z} \times \iint U(\xi, \eta) e^{-j\frac{2\pi}{\lambda z} (x\xi + y\eta)} d\xi d\eta, \tag{4.3}$$

The expression in equation 4.3 is the simple Fourier transform of the input wavefield. Hence, a constant-phase main lobe can be realized at the back focal plane of the lens for centro-symmetric aperture located at $d=f$ illuminated with a plane wave, because the Fourier transform of any real centro-symmetric function is real and centro-symmetric. Our optical configuration stands on this property of lenses.

The schematic representation of the optical configuration is shown in Fig. 4.1. Coherent light from a laser is filtered and collimated by the spatial filter and the lens L1, respectively. The rectangular slit placed after the lens L1 defines the illumination shape and size. By controlling the slit aperture size, the illumination size at the sample plane can be adjusted. An assumption made at this point is that the Gaussian beam diameter incident on the slit is much larger than the slit aperture, and hence the wavefield at the slit plane can be regarded as a plane wave. The optical components in between the light source and the beam-defining slit can be avoided, provided that the beam size at the beam-defining slit is broad enough to satisfy this approximation. The lens L2 generates a Fraunhofer diffraction pattern of the beam-defining slit at its back focal plane. The distance between the slit and lens L2 is equal to the focal length of the lens. Hence, by Eq. 4.3, the wavefield at the back focal plane of the lens has a constant phase within the main lobe. The apodizing slit placed at the back focal plane of the lens L2 functions to remove the side lobes of the Fraunhofer diffraction pattern of the beam-defining slit. The lenses L3 and L4 constitute the so-called 4f imaging system, which forms the image of the apodized wavefield at the back focal plane of the lens L4. Finally, the isolated plane wave illumination is incident on a non-isolated object. The scattered radiation from the sample is collected by the lens L5 placed immediately behind the sample. The lens produces the Fraunhofer diffraction pattern at its back focal plane, where an imaging detector records the pattern.

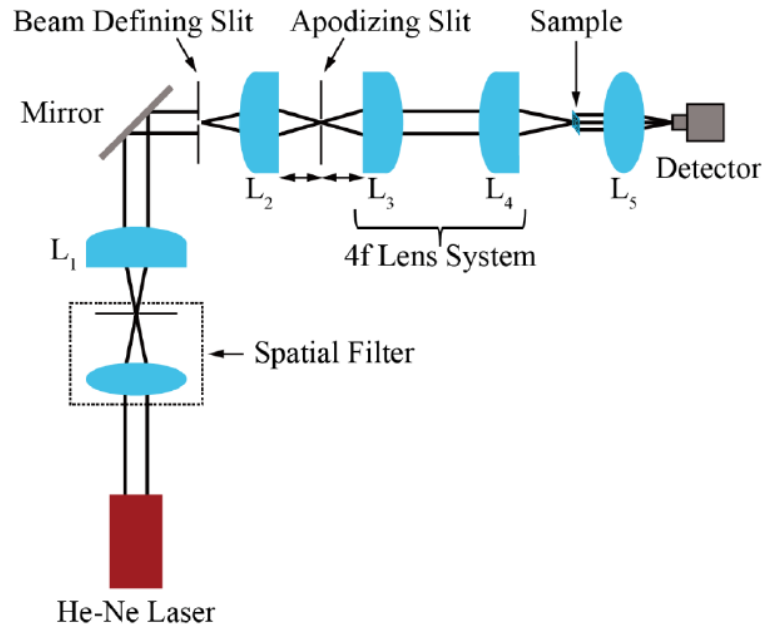


Figure 4.1 Schematic representation of the experimental configuration

4.3 Experimental Results and Discussions

4.3.1 Optical setup

An experimental setup based on the optical design was realized. A He-Ne laser (LASOS Lasertechnik GmbH LGR 7634) emitting light at a wavelength λ of 632 nm with a power of 2 mW was used as a coherent light source. A neutral density filter was placed immediately after the laser system to adjust the light intensity. The parameters of all the lenses used in our experiments are summarized in Table 1. A mirror after the lens L1 was used to change the course of the light by 90° to make the setup compact. The size of the collimated Gaussian beam produced by the spatial filter and the lens L1 was about 15 mm.

Table 4.1 Optical parameters of the lens used in the experiment

Lens	Focal length (mm)	Diameter (mm)
------	-------------------	---------------

L1	100	50
L2	400	50
L3	100	50
L4	100	50
L5	80	50

The aperture size of the beam-defining slit was 1 mm in the both directions with an alignment precision of $\pm 10 \mu\text{m}$. Since the Gaussian beam size is substantially larger than the slit aperture size, the wavefield at the plane of the beam-defining slit can be regarded as a plane wave. We used a Photon Inc. 12-bit USBeamPro charge-coupled device (CCD) Model 2312 with 1360×1024 pixels, each with a size δ of $4.65 \mu\text{m}$, for both recording diffraction patterns and taking bright-field images of the sample. The photographs of the experimental setup are shown in Fig. 4.2.

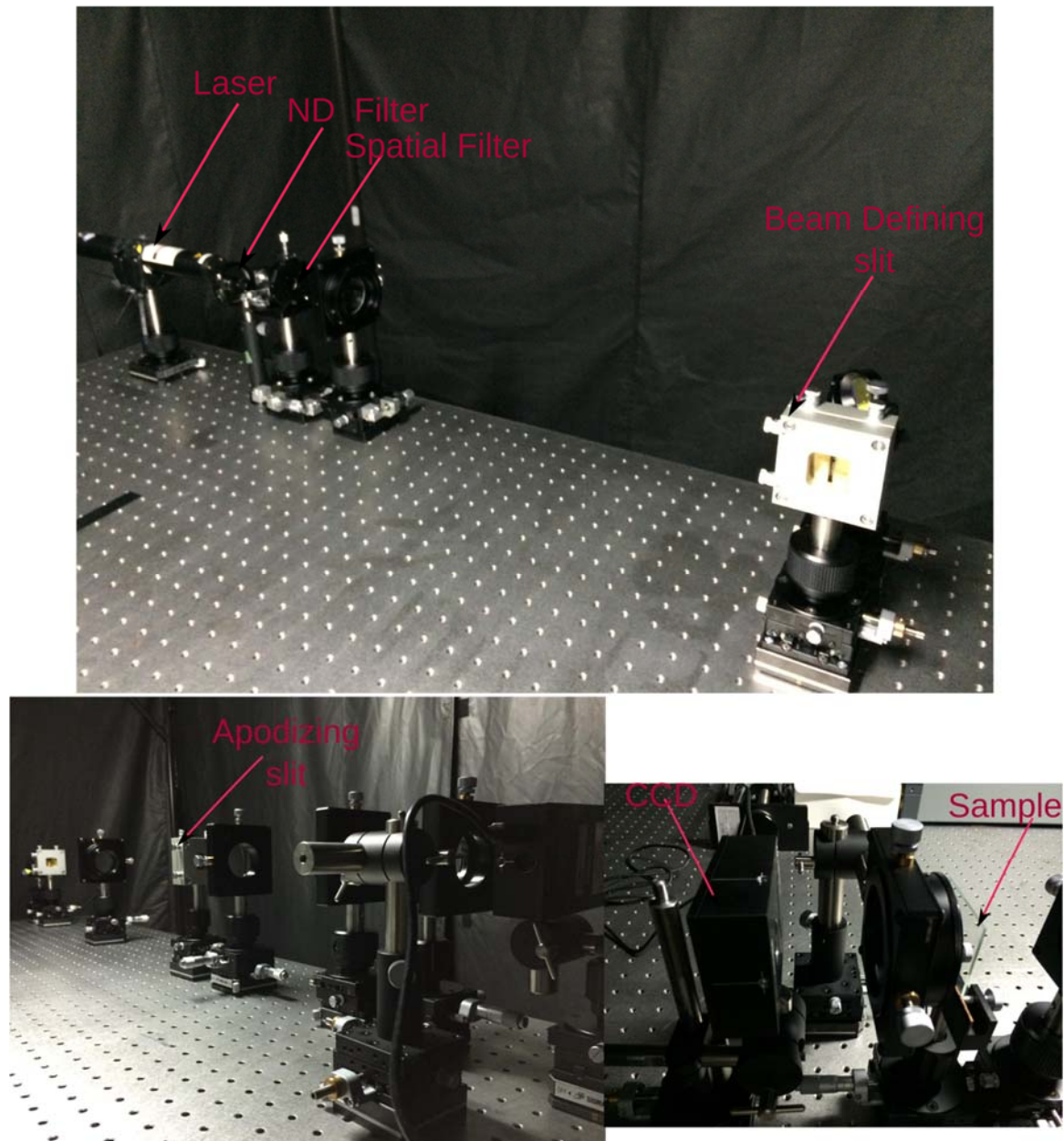


Figure 4.2 Photographs of the experimental setup displaying the optical components

In CDI measurement, the lens L5 was placed physically as close as possible to the sample, and was located at ~ 15 mm from the sample. The lens-detector distance was equal to the focal length of the lens L5 and was 72 mm. In all the results presented in this article, reconstruction was performed using the central $980(N) \times 980(N)$ pixels of the CCD detector. Hence, the pixel size in the real space for all the reconstructed

images presented here is $\lambda l/\delta N \approx 13 \mu\text{m}$, where l is the sample-detector distance and $l=94.2 \text{ mm}$.

The intensity distributions at the sample plane with and without the apodizing slit were measured by the CCD detector in the direct imaging mode. The measurement at various exposure times of 0.1, 1, 10 and 100 ms was made to increase the dynamic range, and were merged into a single intensity distribution.

Fig. 2 shows a comparison of the intensity profiles at the sample plane with and without the apodizing slit. In the measurement with the apodizing slit, the aperture

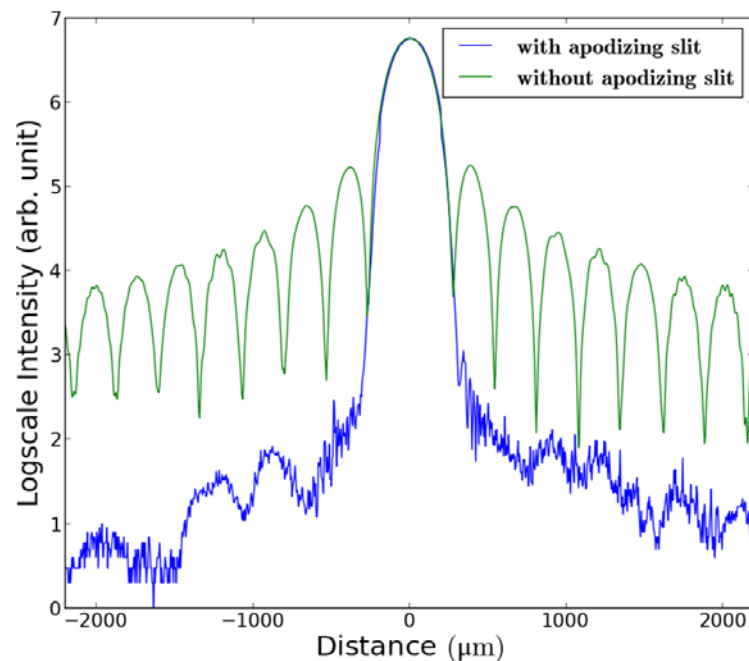


Fig. 4.3 Logarithmic plot of the intensity profiles at the sample plane with and without the apodizing slit.

size and position of the apodizing slit were adjusted while observing the intensity distribution at the sample plane, and were optimized to minimize the side lobe intensities. The precision of apodizing slit adjustment was $\pm 5 \mu\text{m}$. The logarithmic plot in Fig. 4.3 distinctly displays the suppression of the side lobes of the illumination, when the apodizing slit is used at the optimized aperture size and position. The

magnitude of the side lobes in the intensity profile with the apodizing slit has been reduced by approximately three orders of magnitude compared to that without the apodizing slit.

This dramatic decrement in the side lobe intensities of the illumination allows us to perform apodized-illumination CDI. The apodized illumination size a determined from Fig. 4.3 is approximately 538 μm in both dimensions. The oversampling ratio, given by $\sigma = \lambda l / \delta a$, is 21.97.

4.3.2 Imaging of amplitude object

The imaging of an amplitude test pattern was performed in the CDI mode with and without the apodizing slit. A USAF positive resolution target bought from Sigma Koki as shown in Fig. 4.4 (a) was used as a test sample. The diffraction patterns at exposure times of 0.05, 1 and 10 ms were recorded, and a diffraction pattern with a higher dynamic range was tailored by merging them. In merging the diffraction patterns, the intensities at saturated pixels at longer exposures were substituted by the time-scaled intensities of the corresponding pixels with shorter exposures. The diffraction pattern at the shortest exposure time was devoid of saturated pixels. The dark charge noise of the detector at each exposure time was subtracted from the corresponding diffraction pattern before the merging. The center of the diffraction pattern was set to the pixel with the maximum intensity in the diffraction pattern.

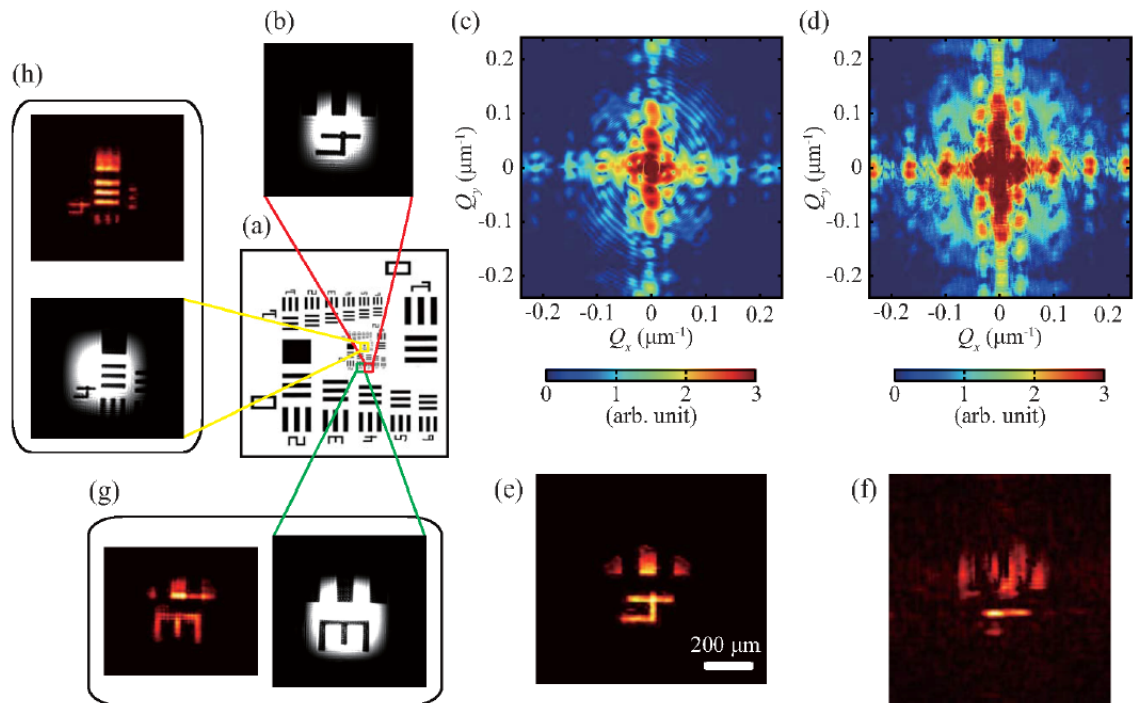


Figure 4.4 (a) A USAF resolution target. (b) The direct image. Merged diffraction patterns (c) with apodizing slit at the optimized aperture size and position and (d) without the apodizing slit. (e) and (f) Reconstructed images from (c) and (d), respectively. (g) and (h) Sets of the direct image and the reconstructed image from other parts of the resolution target.

The reconstruction of the image from the merged diffraction pattern was carried out by using the shrink-wrap hybrid input-output (HIO) algorithm [29]. The algorithm uses a dynamic support constraint unlike the fixed support constraint in the conventional HIO algorithm. The phasing procedure started with a rectangular support with a size slightly larger than the illumination size, and the support was updated by convoluting the reconstructed image with a Gaussian function. The width of the Gaussian function was initially set to 3 pixels, and was reduced by 1% every 10

iterations until the 500th iteration. The threshold for the dynamic update of the support was taken in the range from 8% to 12% of the maximum amplitude of the reconstructed object. After the 500th iteration, the support was held fixed till the 5000th iteration, after which the phasing procedure was ceased. Fig. 4.4 (b) represents the direct image of a part of the sample illuminated by the apodized focused beam. The diffraction patterns with and without the apodizing slit are shown in Fig. 4.4 (c) and 4.4 (d), respectively, and the corresponding reconstructed images in Fig. 4.4 (e) and 4.4 (f), respectively. The dramatic improvement in the quality of the reconstructed image with the apodizing slit can be distinctly observed. Fig. 4.4 (g) and 4.4 (h) are sets of the direct image and the reconstructed image from other parts of the sample. The results prove that the apodization of the illumination is crucial in non-scanning imaging of extended objects.

4.3.3 Imaging of phase object

We also applied apodized-illumination CDI in imaging a phase object. A binary rectangular-groove phase grating was fabricated on the central $3.5 \times 3.5 \text{ mm}^2$ area of a $12 \times 12 \text{ mm}^2$ cover glass using optical lithography. The procedure of optical lithography as shown in Fig 4.5 involves spin coating the photoresist (Tokyo Ohka Kogyo Co., Ltd. OFPR5000LB) on the cover glass, followed by direct laser writing (NEOARK Corp. DDB-201-200). The non-protected region of the cover glass was etched by Reactive Ion Etching (SAMCO Inc. RIE-10NRV). Finally, the photoresist was removed by wet etching with acetone. The lower stripes were designed to be 140 nm deep from the upper stripes. The extinction coefficient of the cover glass at the optical wavelengths is zero. The refractive index of the cover glass was 1.5 and hence the rectangular groove phase grating is expected to produce a phase shift of $\sim 0.22\pi$ rad.

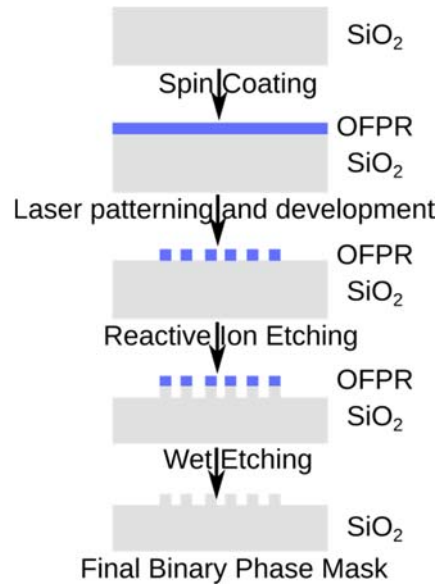


Figure 4.5 Fabrication process of phase object

A traditional bright-field microscopy image (KEYENCE VK-X200) of the phase grating pattern shown in Fig. 4.6 (a) does not provide any contrast as it should be. The inset in Fig. 4.6 (a) is an image of a part of the phase grating pattern taken by a scanning white-light interferometer (Zygo NewView 7300). The widths of the upper and lower stripes were 35 and 45 μm , respectively, and the depth of the groove was ~ 138 nm as determined by the scanning white-light interferometer. Fig. 4.6 (b) and 4.6 (c) are the defocused and focused images, respectively, taken using our optical setup in the direct imaging mode. The diffraction patterns at exposure times of 0.05, 1 and 10 ms were recorded and merged by patching, as explained earlier, to obtain a higher dynamic range diffraction pattern without saturated pixels. Fig. 4.6 (d) shows the merged diffraction pattern. The diffraction pattern consists of periodic maxima along the x-axis as expected from the phase grating pattern. The image was reconstructed from the merged diffraction pattern by using the shrink-wrap HIO algorithm. The threshold for the shrink-wrap algorithm was set to 10% of the maximum of the reconstructed amplitude. The reconstructed image shown in Fig 4.6 (e) was obtained after the 5000th iterations. The reconstructed image obtained in the

CDI mode and the defocused image in the direct imaging mode was found to be in good agreement. Fig. 4.6 (f) is the line profile along the dashed line in the reconstructed image. The full width at half maximum (FWHM) of the upper and lower stripes as determined from the reconstructed images was 36 μm and 45 μm respectively. The line profile agrees well with the fabricated pattern proving the reliability of the method in imaging phase objects.

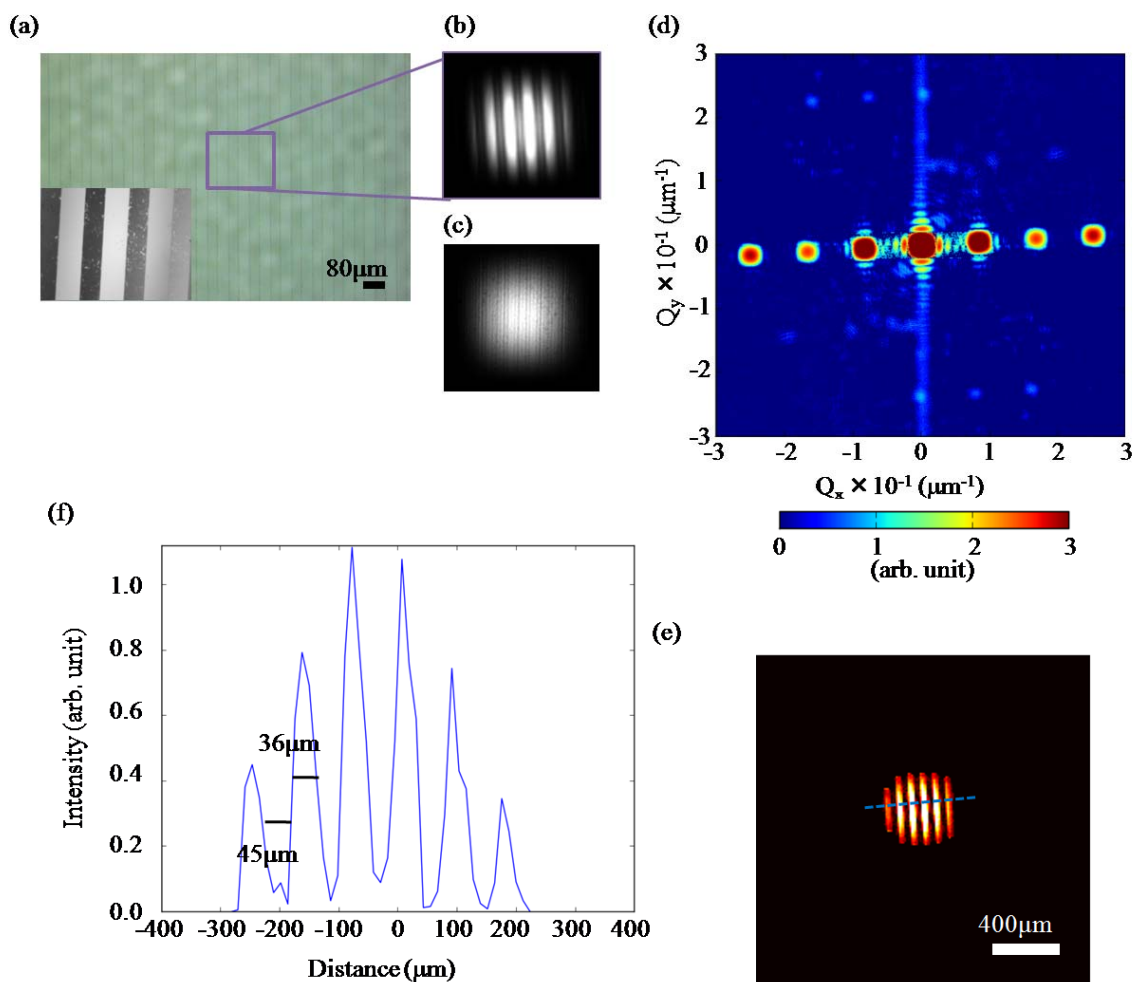


Fig 4.6. (a) Optical microscope image of a binary phase grating pattern; the inset is the image from a scanning white-light interferometer. (b) Defocused and (c) focused images in the direct imaging mode. (d) Merged diffraction pattern. (e) Reconstructed image

4.4 Conclusions

To summarize, we have demonstrated a non-scanning CDI of extended objects with apodized illumination. In the process, we have realized isolated apodized illumination with a constant phase by using a specially designed optical configuration. The optical system is composed of a beam defining slit illuminated by a plane wave at the front focal plane of a lens, an apodizing slit at the back focal plane of the lens, and a subsequent 4f imaging system. The apodizing slit successfully reduced the side lobe intensities approximately by three orders of magnitude as compared to the case without the apodizing slit.

In apodized-illumination CDI experiment, we used a USAF positive resolution target as an amplitude object and a binary rectangular-groove grating as a phase object. The grating pattern was fabricated by optical lithography. In recording coherent diffraction patterns, we merged CCD data with different exposure times to increase the dynamic range. The shrink-wrap HIO algorithm was used for image reconstruction. For the both samples, the dramatic improvement in the quality of the reconstructed image with the apodizing slit was observed.

We believe that the method can be expanded to quantitative phase imaging of cells and tissues. The non-scanning nature of the method will be useful in the quantitative study of fast cellular activities, such as membrane fluctuations [30]. Our results also proved the feasibility of the imaging of extended objects with x-ray free-electron lasers [31–33], where other methods fall short. The concept of the spatially localized illumination in apodized-illumination CDI can also be transferred to the ptychography community to realize aperture-less ptychography.

References

- [1] F. Zernike, *Physica* **9**, 686–698 (1942).
- [2] F. Zernike, *Physica* **9**, 974–986 (1942).
- [3] E. M. Slayter and H. S. Slayter, *Light and Electron Microscopy* (Cambridge University, 1993).
- [4] R. Barer, *Nature* **169**, 366–367 (1952).
- [5] Z. Wang et al., *Opt. Express* **19**, 1016–1026 (2011).
- [6] N. T. Shaked, *Opt. Lett.* **37**, 2016–2018 (2012).
- [7] T. E. Gureyev and K. A. Nugent, *Opt. Commun.* **133**, 339–346 (1997).
- [8] J. Miao et al., *Nature* **400**, 342–344 (1999).
- [9] I. Robinson and R. Harder, *Nat. Mater.* **8**, 291–298 (2009).
- [10] J. Miao et al., *Proc. Natl. Acad. Sci. U.S.A.* **100**, 110–112 (2003).
- [11] D. Shapiro et al., *Proc. Natl. Acad. Sci. U.S.A.* **102**, 15343–15346 (2005).
- [12] Y. Nishino et al., *Phys. Rev. Lett.* **102**, 018101 (2009).
- [13] J. Nelson et al., *Proc. Natl. Acad. Sci. U.S.A.* **107**, 7235–7239 (2010).
- [14] H. Jiang et al., *Proc. Natl. Acad. Sci. U.S.A.* **107**, 11234–11239 (2010).
- [15] J. M. Rodenburg et al., *Phys. Rev. Lett.* **98**, 034801 (2007).
- [16] P. Thibault et al., *Science* **321**, 379–382 (2008).
- [17] M. Dierolf et al., *Nature* **467**, 436–439 (2010).
- [18] K. Giewekemeyer et al., *Proc. Natl. Acad. Sci. U.S.A.* **107**, 529–534 (2010).
- [19] A. M. Maiden et al., *Opt. Lett.* **35**, 2585–2587 (2010).

- [20] J. Marrison et al., *Sci. Rep.* **3**, 2369 (2013).
- [21] D. A. Shapiro et al., *Nat. Photonics* **8**, 765–769 (2014).
- [22] L. Shemilt et al., *Biophys. J.* **108**, 706–713 (2015).
- [23] T. Kimura et al., *Opt. Express* **21**, 9267–9276 (2013).
- [24] I. Robinson et al., *Opt. Express* **11**, 2329–2334 (2003).
- [25] R. L. Sandberg et al., *Phys. Rev. Lett.* **99**, 098103 (2007).
- [26] C. G. Schroer et al., *Phys. Rev. Lett.* **101**, 090801 (2008).
- [27] Y. Takahashi et al., *Phys. Rev. B* **80**, 054103 (2009).
- [28] J. Goodman et al., *Introduction to Fourier Optics* (Roberts and Company, 2004).
- [29] S. Marchesini et al., *Phys. Rev. B* **68**, 140101 (2003).
- [30] J. Miao et al., *Phys. Rev. B* **68**, 012201 (2003).
- [31] G. Popescu, *Quantitative Phase Imaging of Cells and Tissues* (McGraw–Hill, 2011).
- [32] M. M. Seibert et al., *Nature* **470**, 78–81 (2011).
- [33] J. Pérez and Y. Nishino, *Curr. Opin. Struct. Biol.* **22**, 670–678 (2012).
- [34] T. Kimura et al., *Nat. Commun.* **5**, 3052 (2014)

Chapter V. Generation of apodized x-ray illumination and its application to scanning and diffraction microscopy

5.1 Introduction

Nano-scale x-ray imaging has undergone an enormous development largely due to the progress made in x-ray focusing optics as well as light sources [1, 2]. The utilization of focused x-ray illumination in various forms of x-ray microscopic techniques, such as scanning x-ray fluorescence microscopy (SXF_M) [3-7] and coherent diffractive imaging (CDI) [8-10], has become routine and has served to improve the performance of these techniques [11-12]. The focused beam profile is usually accompanied by the side-lobes in addition to the main lobe, and the spatially extended nature of focused illumination due to the side-lobes either decline or limit their performances. For instance, the presence of the side-lobes in the focused illumination declines the practically obtainable resolution of the images in SXFM. Also, in the realization of CDI of extended objects, both in the scanning and non-scanning mode, localized illumination is indispensable. For the extension of the applications of these techniques, elimination or substantial suppression of side-lobe intensities in the focused illumination is a must. Recently, the authors have proposed an optical design to generate spatially-localized focused illumination, where side-lobe intensities are largely suppressed, and have presented a numerical simulation on the use of such apodized illumination in imaging non-isolated objects by non-scanning CDI [13]. In this article, we present the realization of such optical setup employing a two-stage deformable Kirkpatrick-Baez (KB) mirror system to generate the apodized illumination. As proof-of-principle experiments, we also demonstrate the enhancement of the resolution in SXFM and the imaging of an extended test object by apodized-illumination CDI.

Before going into the details of the experimental results, we will briefly introduce the synchrotron light source and Focusing optics which is the key components of the experiments discussed in this chapter.

5.2 Synchrotron X-ray Source

X-rays are electromagnetic radiation with wavelength of the order of Angstrom. The sources generating x-rays have seen a significant development since its discovery in 1895 by Roentgen. The Coolidge tube x-ray source and the rotating anode are the first generation of the x-rays. Although these sources are used for various scientific and medical purposes, the synchrotron x-ray sources dominate modern scientific research with x-rays.

Synchrotrons are special type of accelerators in which particles are accelerated in a circular arc. If the particles accelerated are charged such as electrons or positrons, then by the fundamental theory of electromagnetism, radiations are generated from such accelerators. This radiation is called synchrotron radiation. Usually, the charged particles in synchrotrons are rotated with uniform energy in a storage ring. These charged particles are then allowed to pass through the alternating magnetic field which oscillates the charged particles and hence finally a radiation is emitted. The quality of such radiations depends on several aspects which are collectively summarized as the Brilliance of the source and is defined as follows,

$$Brilliance = \frac{Photons/sec}{(mrad)^2(mm^2SA)(0.1\%BW)} \quad 5.1$$

SA is the source area and BW is the bandwidth of the source. Higher the Brilliance better the sources are. Hence, there is an ever-growing interest in the development of x-ray source with higher brilliance. The coherence properties of the synchrotron radiation, which are of particular importance for coherent diffraction imaging, follow the definition of coherence provided in the chapter II.

5.3 X-ray Mirrors

With the development of the electromagnetic radiation at shorter wavelength, the optical devices to collect, guide, focus, such radiation becomes indispensable for the broader applications of such radiations. Though, such optical devices at visible light wavelengths are well developed, these techniques cannot be immediately translated to the shorter wavelengths due to complex light-matter interaction. For instance, the refractive index of x-rays in the materials is slightly below unity which makes the use of refractive lens, highly successful at longer wavelengths, challenging to either focus light or image an object. This was also one of the major hurdles in realizing the lens-based x-ray microscope.

In 1948, Paul Kirkpatrick and A. V. Baez introduced a total-external reflection based concave mirror which could produce a line focus of a point object. They also displayed that arranging two such mirrors in orthogonal alignment could produce a point image of a point object and extended image of an extended object.

The fundamental principle behind the KB mirror system is the total external reflection. When a broadband x-ray beam is incident on the smooth surface at an angle smaller than the critical angle, the wavelengths larger than the cutoff wavelength will be reflected with almost complete efficiency. The cutoff wavelength is given by,

$$\lambda_{cutoff} = (c/e)(\pi m / \rho)^{1/2} \quad 5.2$$

Where c represents the speed of light, e is the electronic charge, m is the electronic mass and ρ is the charge density.

The critical angle required for the total external reflection for the mirrors is given by,

$$\theta_c = \sqrt{2\delta} \quad 5.3$$

Where δ is the component of the real part of the refractive index which reduces the refractive index to less than unity. The value of δ in solids is of the order of 10^{-5} .

Hence, the critical angle is of the order of mill-radian.

The efficiency of the reflection based mirrors are governed by the several degrees of freedom such as the mirror figure, the surface smoothness, the precision of the alignment during experiments and the involved metrological techniques. Over last two decades significant improvement has been seen in the realization of near-ideal x-ray reflection mirrors.

5.4 Experimental setup

We performed an experiment to generate a focused illumination with suppressed side-lobe intensities at the experimental hutch 3 (EH3) of BL29XU, an undulator beamline with an overall length of 1km, at SPring-8 [14]. A schematic of the optical system is shown in Fig. 5.1. The optical system is comprised of two pairs of deformable mirrors [15], each aligned in the Kirkpatrick-Baez (KB) geometry [16].

A slit in the transport channel of the beamline, the TC1 slit, defines the beam shape and size. The beam defined by the TC1 slit behaves as the virtual source for the constructed optical system. The coherence area at the entrance of the two-stage deformable KB mirror system, which is located ~ 50 m downstream of the TC1 slit, can be adjusted by varying the aperture size of the TC1 slit. For diffraction-limited focusing, the coherence area larger than the entrance aperture

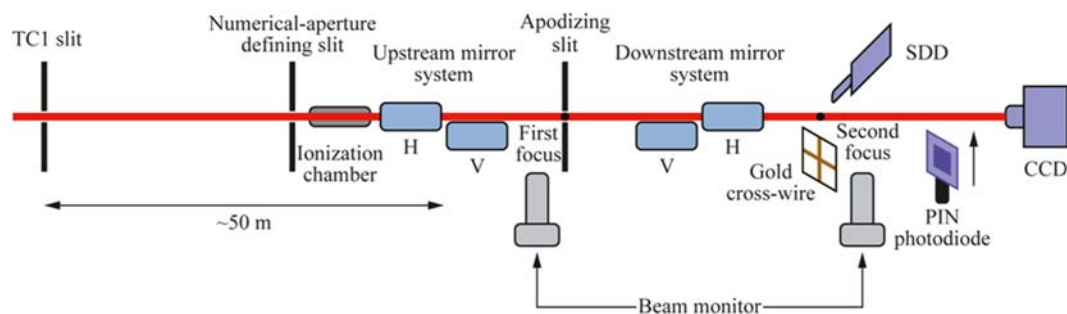


Figure 5.1 Schematic of the experimental setup

of a focusing optics is required. A numerical-aperture defining slit was installed just before the two-stage deformable KB mirror system to regulate the entrance aperture.

An ionization chamber immediately behind the numerical-aperture defining slit provides the incident photon flux.

The deformable KB mirror system closer to the TC1 slit will be referred to as the upstream mirror system and the farther one the downstream mirror system. The upstream mirror system with a one-dimensional elliptical shape is designed such that its front focus is at the TC1 slit. At the back focal plane of the upstream mirror system, we placed an apodizing slit. The apodizing slit functions to get rid of the side-lobe intensities of the beam focused with the upstream mirror system. A detailed

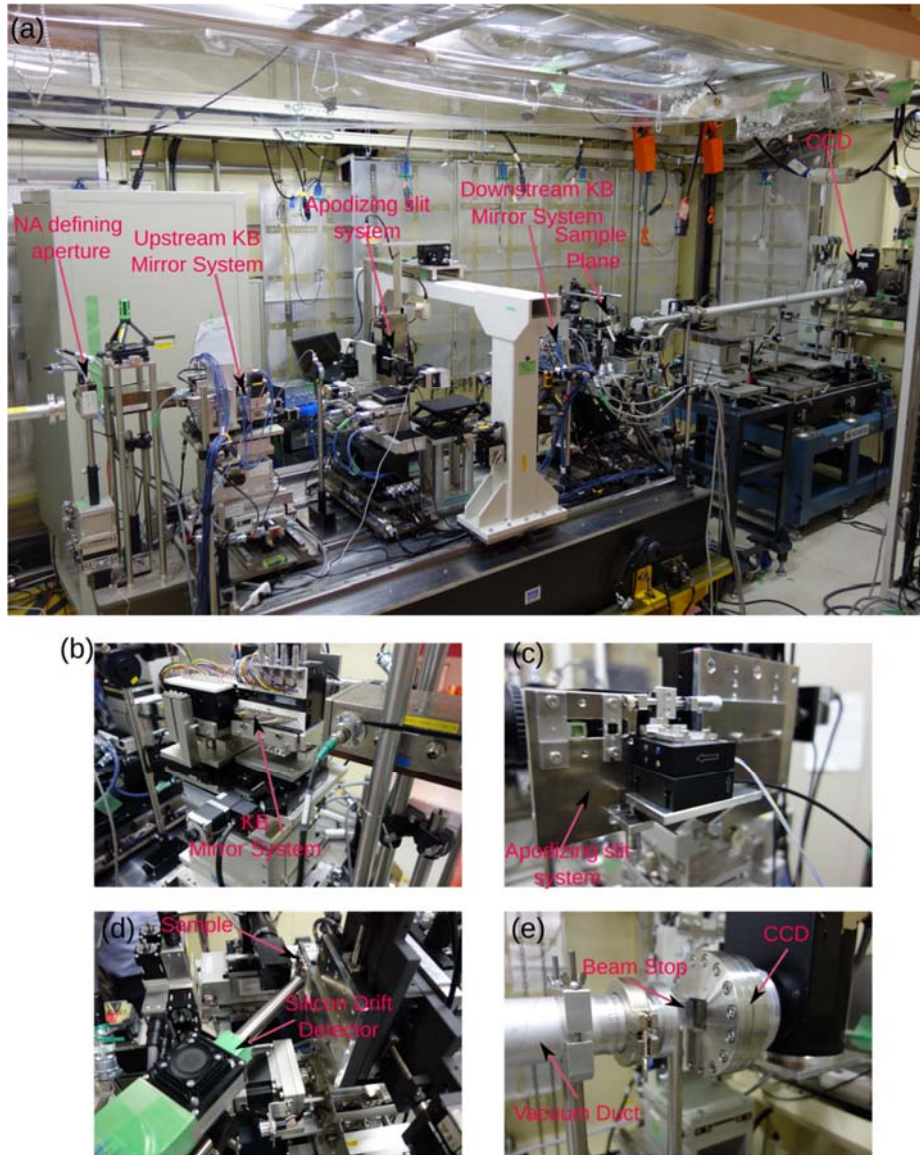


Figure 5.2 (a) Photograph of the entire experimental set-up. Close-up view of (b) the focusing KB Mirrors (c) the apodizing slit system (d) sample and fluorescence detector (e) beam stop and CCD.

discussion on the design, construction and the alignment procedure of the apodizing slit will be presented at the later part of this article. The front focus of the downstream mirror system was designed to coincide with the back focal plane of the upstream mirror system, and the common focus is hereafter called the first focus. The image of the beam profile in the first focal plane is then formed at the back focal plane of the downstream mirror system, the second focal plane. The side-lobe intensities at the

second focus can be suppressed by optimizing the aperture size and position of the apodizing slit. The illumination with suppressed side-lobe intensities at the second focus will be hereinafter termed as apodized illumination. At the second focal plane, we installed xz translation stages with a positional precision of 1 nm (the 1nm-precision-stages), on which the samples and the gold cross-wire for focused-beam profile measurement are mounted.

The optical system shown in Fig 5.2 realizes variable focal spot size at the fixed sample position by changing the first focal position with the deformable mirrors. We set a limit on the range of the first focal position so that the convergence angle of the upstream mirror does not exceed the angular acceptance of the downstream mirror. The convergence angle of the upstream mirror and the angular acceptance of the downstream mirror are given by a_u/f_{ub} and a_d/f_{df} , respectively. Here, f_{ub} is the back focal length of the upstream mirror, and f_{df} is the front focal length of the downstream mirror. a_u and a_d is the aperture sizes of the upstream and downstream mirrors, respectively, and are expressed as $a_u = l_u \theta_u r_a$ and $a_d = l_d \theta_d$, where l_u and l_d are the lengths and θ_u and θ_d are the glancing angles of the upstream and downstream mirrors, respectively. r_a is the aperture ratio set by the numerical aperture defining slit. Since the length and the glancing angle are the same for all the four mirrors in our system, $l_u = l_d = 100$ mm and $\theta_u = \theta_d = 4$ mrad, the optical system was so designed to keep f_{df} is equal to or shorter than f_{ub} . Different focal spot sizes at the sample position were used for the SXFM and CDI experiments. The parameters of the mirror systems for both the cases are summarized in Table 5.1.

Table 5.1 The optical parameters of the mirrors

	Glancing	SXFM Measurement	CDI Measurement

	angle	Front focal length	Back focal length	Front focal length	Back focal length
Upstream mirror system (Horizontal)	4 mrad	~50 m	1250 mm	~50 m	750 mm
Upstream mirror system (Vertical)	4 mrad	~50 m	1120 mm	~50 m	620 mm
Downstream mirror system (Horizontal)	4 mrad	250 mm	300 mm	750 mm	300 mm
Downstream mirror system (Vertical)	4 mrad	120 mm	430 mm	620 mm	430 mm

The optical system also contains retractable beam monitors at the first and second focuses used in the alignment and deformation of the mirrors. These beam monitors also facilitate the alignment of the apodizing slit and coarse determination of the sample positions. An escapable PIN photodiode is placed 0.4 m downstream of the sample plane and is used to measure the beam profiles at the back focal planes of both the mirror systems by the knife-edge scan. A silicon drift detector (SDD), for the detection of fluorescent x-rays, was placed off-axis and physically close (~15 mm) to the sample. In the CDI mode, a charge-coupled device (CCD) is placed at 2.51 m downstream of the sample plane in the Fraunhofer regime to satisfy the oversampling condition and is used to record the coherent x-ray diffraction (CXD) patterns. A beam-stop is placed immediately in front of the detector to prevent the detector from the potential damage due to the intense direct x-ray beam reflected from the optical system. The path in between the sample and the detector was evacuated to a pressure

of the order of 10^{-3} Pa. The PIN photodiode and the SDD were escaped out of the x-ray path during the CDI measurement.

5.5 Design of the apodizing slit system and the apodization experiment

In designing the apodizing slit, a precision substantially smaller than the focused beam size is required. Additionally, all the blades of the apodizing slit need to be within the depth of focus of the upstream mirror system. The shortest depth of focus of the upstream mirror system used in our experiments is 1.8 mm. Fig. 5.3 shows a drawing of the entire structure of the apodizing slit system we designed.

The apodizing slit rests on the aluminum support, which is mounted on a two-axis translation stages with a positional precision of 5 nm. Four gold wires with a diameter of 200 μm are used as the blades of the apodizing slit and are installed as two pairs of a perpendicular cross-wire to define the rectangular aperture. One of the cross-wires is fixed to the aluminum support. The aperture size can be changed by translating the other pair of the cross-wire attached to xz piezo stages (Physik Instrumente), which is connected to the aluminum support through a flexure hinge. The travel range of both the piezo stages is 100 μm . There are also three micrometer-heads for coarse adjustment of the slit aperture and the parallelism of the two cross-wires.

The aperture size of the apodizing slit was optimized in two steps. In the first step, the aperture size was coarse-tuned by using the micrometer heads before installing the apodizing slit system in EH3. The coarse tuning involves the reduction of the aperture size to less than $100 \mu\text{m} \times 100 \mu\text{m}$, a constraint set by the travel range of the xz piezo stages used. In addition, the parallelism of the two cross-wires was optimized with a precision better than 2 mrad by using two micrometer-heads beneath the xz piezo stage. All the four gold wires were placed within 800 μm along the x-ray path as

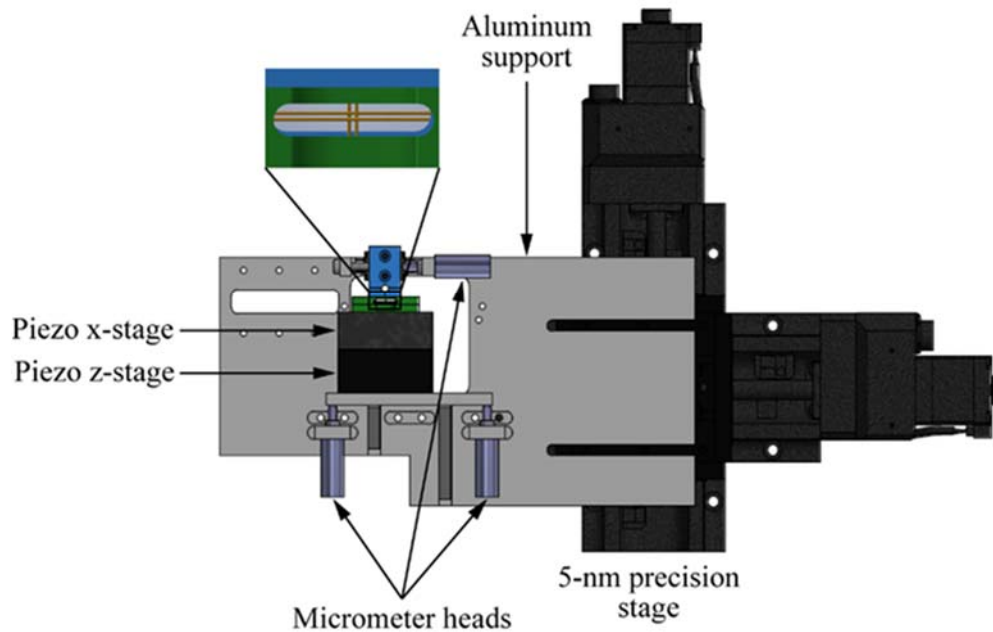


Figure 5.3 Drawing of the apodizing slit system. The zoomed image shows the arrangement of the four gold wires used as the slit blades.

confirmed by using the beam monitor at the first focus, which is smaller than the depth of focus of the upstream mirror system.

In the second step, the aperture size and the position of the apodizing slit was adjusted on-line by using the piezo stages with measuring the beam profile at the first and the second focuses. The beam profiles at the first and the second focuses were measured by employing the bright field and dark field wire-scanning method [17] respectively, using the PIN photodiode. Determination of the rough positions of the apodizing slit was done by observing the first minimum in the illumination profiles measured at the first focus. The apodizing slit size was then optimized by observing the dark-field wire scanning profiles measured at the second focus.

For apodization and SXFM experiments, x-rays with photon energy of 10 keV and a virtual source (TC1 slit) size of $10\ \mu\text{m} \times 10\ \mu\text{m}$ were used. The measured focal spot sizes (full width at half maximum) at the back focal plane of the upstream and downstream mirror system were $650\ \text{nm} \times 1500\ \text{nm}$ and $1000\ \text{nm} \times 1800\ \text{nm}$, respectively. The aperture size and position of the apodizing slits were optimized with an accuracy of $\pm 200\ \text{nm}$. A comparison of the horizontal intensity profile at the second focus with and without the apodizing slit is shown in Fig. 5.4. The profiles were measured by dark field wire scanning method with scan step size of $100\ \text{nm}$. It is apparent from the graph that the use of the apodizing slit made the illumination profiles smoother and the side-lobe intensities were suppressed.

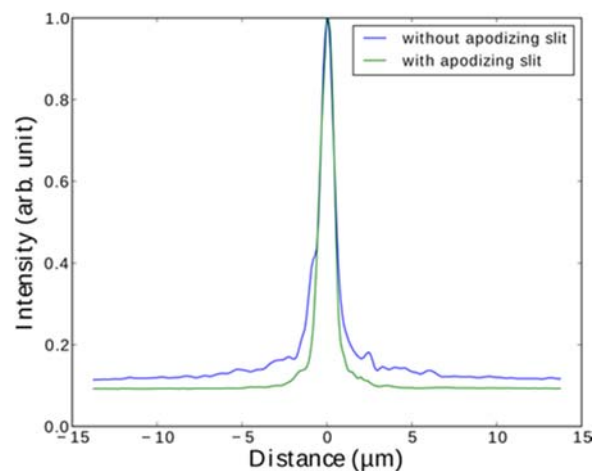


Figure 5.4 A comparison of the experimental profiles at the back-focal plane of the downstream mirror system with and without the apodizing slit

5.6 SXFM with apodized illumination

SXFM provides elemental maps by detecting characteristic fluorescent x-rays at different sample positions. We performed SXFM measurement for a chromium mesh pattern by using the focused apodized illumination.

An optical micrograph of the chromium mesh pattern is shown in Fig. 5.5 (a). The mesh pattern is composed of $5\ \mu\text{m}$ half-pitch line and space patterns in both directions

and fabricated on a 200 nm thick silicon nitride (SiN) membrane substrate using electron beam lithography. We employed the lift-off process, which involves spin-coating of the photo-resist (ZEP 520A), electron beam writing (ELIONIX ELS-F125), development, deposition of the chromium, and finally the wet-etching using Dimethylacetamide (ZDMAC). The chromium was deposited by a compact sputter system (ULVAC ACS-4000-C3-HS) and the thickness of the deposited layer is ~ 5 nm. The patterned area on the SiN membrane was $500 \mu\text{m} \times 500 \mu\text{m}$.

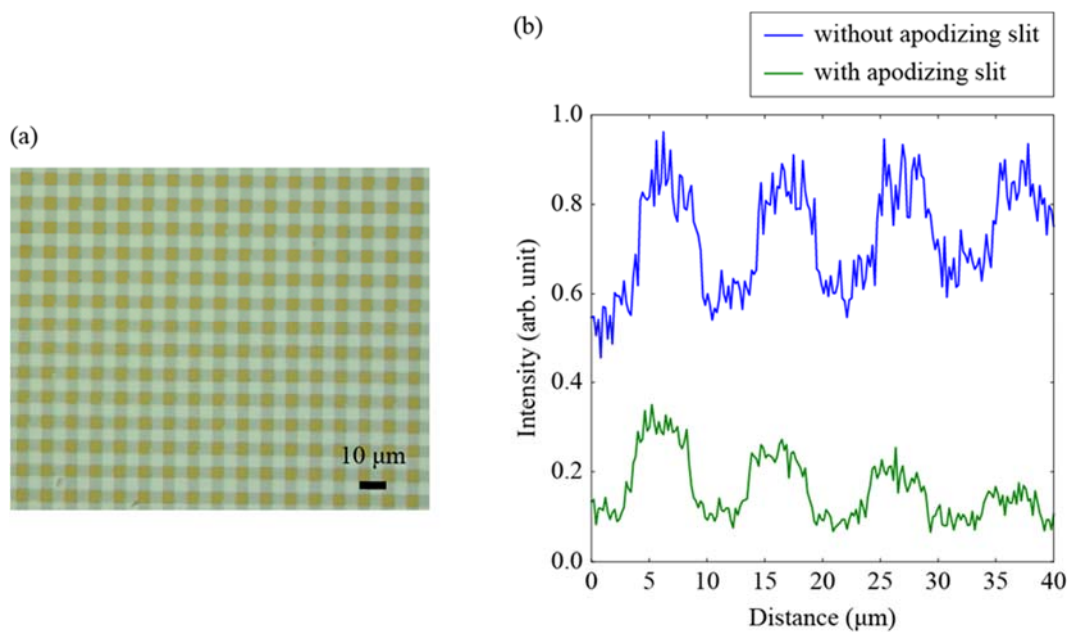


Figure 5.5 SXFM experiment. (a) Optical micrograph of the chromium mesh pattern used as a test object in SXFM measurement. (b) One dimensional map of Cr $K\alpha$ fluorescence of the test object measured by SXFM.

The fabricated test pattern was mounted on the 1-nm-precision-stage in the sample plane. The x-ray fluorescence from the chromium was measured by the SDD (X-Flash Detector type 1201, Röntec Co. Ltd.). The sample was scanned with the focused beam with a step size of 200 nm. At each position, the sample was exposed for 5 s, which was found to be long enough to collect adequate signals to generate the contrast in the image. The line profiles of Cr $K\alpha$ fluorescence along the horizontal direction of the

sample with and without the apodizing slit are shown in Fig. 5.5 (b). With the employment of the apodizing slit, the background noise was significantly reduced. Also, the image measured with the optimized apodizing slit has slightly sharper edges than the image without the apodizing slit providing an indication of improvement in the resolution of the image with the apodized illumination. Defining contrast as the ratio of the maximum intensity and the minimum intensity in the profiles, we obtain contrast values for profiles with apodizing slit and without apodizing slit as 5.2 and 2.1 respectively. Hence, an enhancement of the contrast by a factor of ~ 2.5 has been achieved by using the apodizing slits.

A numerical simulation has been performed to make a comparison with the experimental observation. The results of the simulation have been summarized in the Fig. 5.6. The intensity distribution obtained by wave optical simulation, at the sample plane, with and without apodization is shown in Fig. 5.6 (a) and 5.6 (b) respectively. A binary mesh pattern, shown in Fig. 5.6 (c), was taken as the sample in order to mimic the experimental environment. The sample was scanned along horizontal direction, with illuminations shown in Fig. 5.6 (a) and 5.6 (b), in 85 steps. The line profile thus obtained is plotted in Fig. 5.6 (d). It is obvious from the line profiles that the background intensities have been significantly suppressed with apodized illumination. Also as expected, the line profiles with the apodized illumination are observed to be sharper than the one without apodization. These observations are consistent with our experimental results.

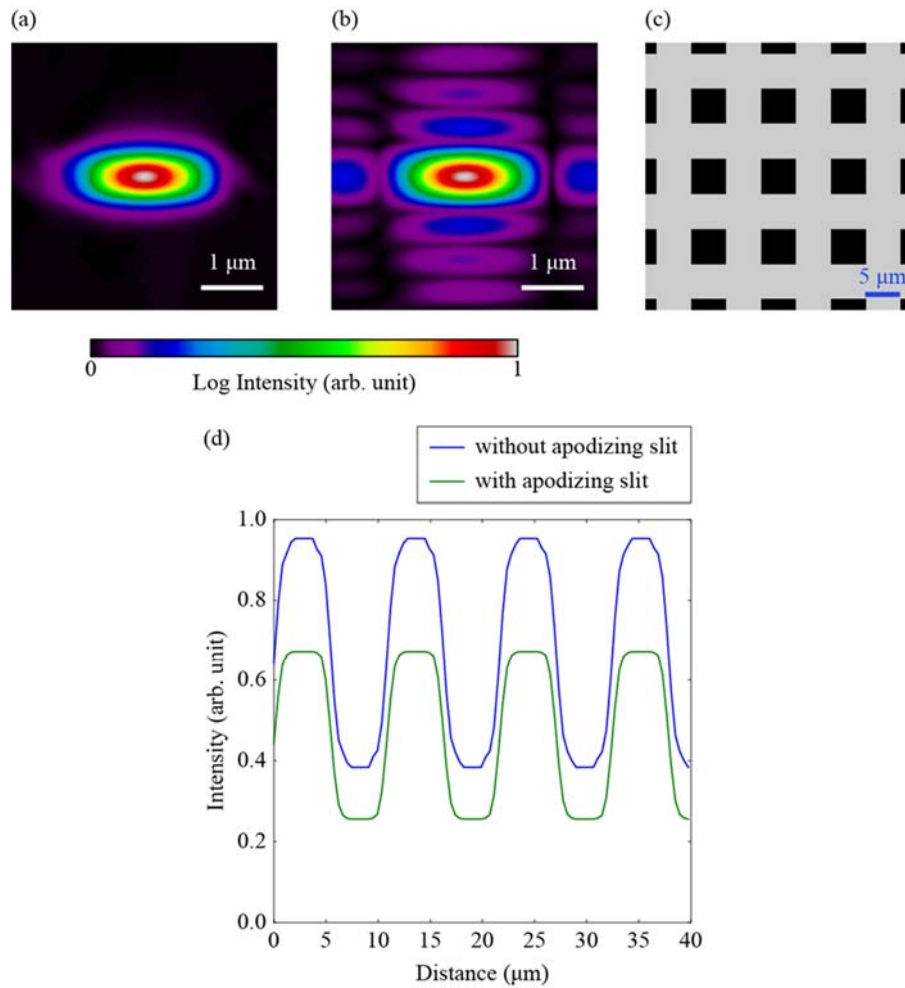


Figure 5.6 Numerical simulation of SXFM. Illumination at the sample plane obtained by wave-optical simulation (a) with and (b) without apodizing slit. (c) Binary mesh pattern used as a sample. (d) Horizontal line profiles of simulated SXFM data obtained us

5.7 Coherent diffractive imaging with apodized illumination

We performed a CDI experiment for a 1- μm grid pattern in the NTTAT-test chart (NTT-AT XRESO-50HC). In the grid pattern, the width of each line is 250 nm and the distance between two adjacent lines is 750 nm. The x-ray photon energy was 9 keV, and the virtual source size was $20 \mu\text{m} \times 20 \mu\text{m}$. The mirror parameters used for the CDI experiment as shown in Table I produces the narrowest x-ray beam for the designed optical system. The scattering from the edge of the mirror can deteriorate the

quality of the apodized illumination. In order to avoid such circumstances, the numerical-aperture defining slit was adjusted such that only sixty percent of the total effective aperture of the mirror is illuminated. For the optical configuration used for the CDI experiment, the measured spot size (full width at half maximum) at the first and second focuses are $600 \text{ nm} \times 400 \text{ nm}$ and $400 \text{ nm} \times 650 \text{ nm}$ respectively. In the measurement of diffraction patterns, a pair of x-ray cross slits was placed immediately before the sample in order to cut-off the parasitic scattering from the optical system. Diffraction patterns were recorded with an x-ray CCD (Princeton Instruments PI-LCX: 1300) consisting of 1340×1300 pixels, each of area $20 \text{ } \mu\text{m} \times 20 \text{ } \mu\text{m}$. The CCD, operated in vacuum, was cooled to a temperature of -100°C with liquid nitrogen in order to reduce the dark current noise. The sample detector distance (l) in the experimental results presented below was 2.51 m. With this optical configuration the minimum oversampling ratio given by $\sigma = \lambda l / \delta a$, is ~ 13 , where λ is the x-ray wavelength, δ is the pixel size and a is the largest dimension of the incident illumination at the sample plane. We used the CXI data in the central 1200×1200 pixel of the CCD. The diffraction patterns shown in this article are those after subtraction of the background noise and binning by a factor of two in each direction. The pixel size of reconstructed images is $\sim 14 \text{ nm}$ as determined from the experimental geometry.

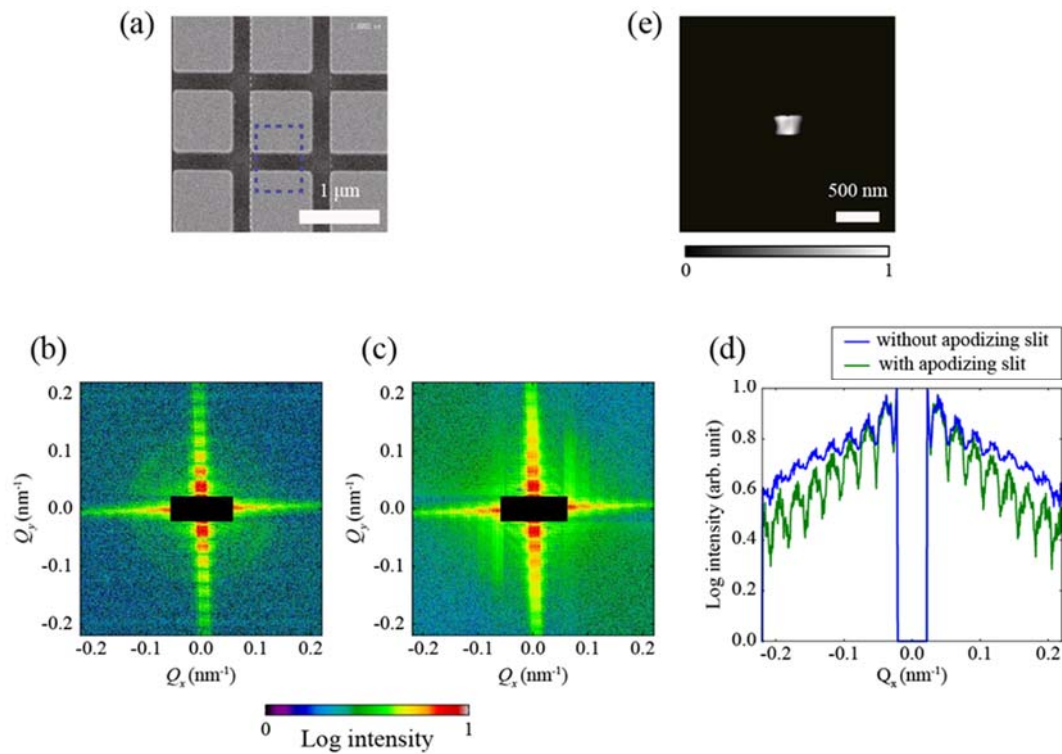


Figure 5.7 CDI experiment (a) The 1- μm grid pattern in the NTTAT-test chart used as a sample in CDI experiment. CXD patterns (b) with the apodizing slit at the optimized aperture size and position and (c) without the apodizing slit. (d) Comparison of the visibility of the fringes in the CXD patterns (b) and (c). The axes Q_x and Q_y in the graphs are defined as $Q_x = \frac{2\pi}{\lambda} \sin \theta_x$ and $Q_y = \frac{2\pi}{\lambda} \sin \theta_y$, respectively, where λ is the wavelength and θ_x and θ_y are the scattering angles along x and y direction. (e) Reconstructed image from the CXD pattern shown in (b) with apodizing slit.

The diffraction pattern, with and without the apodizing slit is shown in Fig. 5.7 (b) and 5.7 (c) respectively. The total exposure time for each diffraction pattern was 600 s. The line profile shown in Fig. 5 (d) is plotted along the vertical fringe in the diffraction patterns. The profiles clearly show an improvement in the visibility of the diffraction pattern with apodized illumination. We performed a numerical study to verify the effect of the apodization on the fringe visibility of the diffraction pattern.

Fig. 5.8 presents the summary of the numerical study. The intensity distribution used for this study is same as the one used for numerical simulation of SXFM. The binary mesh pattern shown in Fig. 5.8 (a) is used as the sample for our study. Fig. 5.8 (b) and 5.8 (c) shows the exit wave with and without apodized illumination. The simulated diffraction pattern with and without apodized illumination are shown in Fig. 5.8 (d) and 5.8 (e) respectively. The line profiles along the vertical fringe of the diffraction patterns are shown in Fig. 5.8 (f). From the figure, it is apparent that the visibility of the diffraction pattern improves significantly when the sample is illuminated with apodized illumination. The numerical results supports well to our experimental observation.

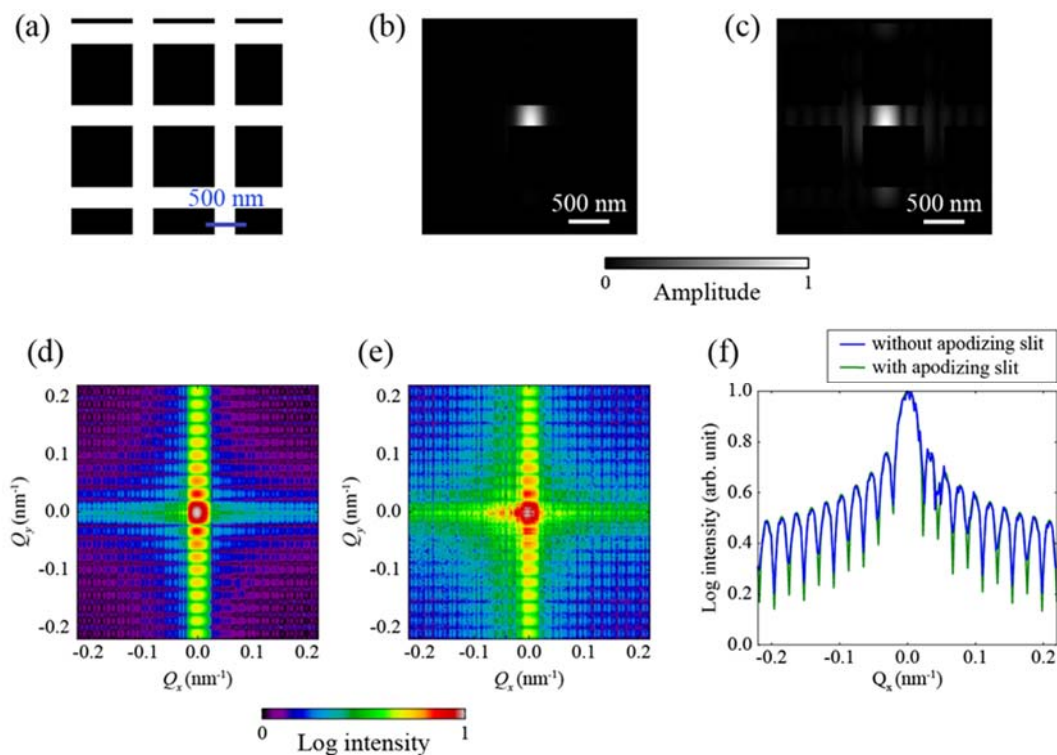


Figure 5.8 Numerical simulation of CDI. (a) Binary mesh pattern used as a sample. Exit wave from the sample using wave-optically simulated illumination (b) with and (c) without apodizing slit. Simulated diffraction patterns (d) obtained from (b); and

(e) obtained from (c). (f) The line plot along the vertical fringe through the centre in the diffraction patterns (d) and (e).

We used a combination of shrink-wrap hybrid input-output algorithm (HIO) [18] and error reduction (ER) algorithm for image reconstruction from the diffraction pattern. The support size was initially set to be slightly larger than the illumination size. The support was then gradually updated by convoluting the reconstructed image with a Gaussian function. The width of the Gaussian function was initially set to be 2.0 pixels and was reduced by 1% every 50 iterations. The threshold for the dynamic support was set to 8% of the maximum of the reconstruction. The reconstructed image in Fig. 8 (b) is obtained after a total of 10000 iterations, of which first 5000 were performed with shrink-wrap HIO and the last 5000 with shrink-wrap ER. The line pattern in the reconstructed image is in agreement with the line in the 1- μm grid pattern as shown in Fig. 8 (a). The dotted line in Fig. 8 (a) represents the position of the focused illumination.

5.8. Conclusions

In summary, we have constructed a two-stage deformable KB mirror system to generate apodized illumination. The apodized illumination thus generated has a smoother profile compared to the one without the apodizing slit. In the process, we have designed, constructed and tested a compact x-ray cross-slit with precisely controllable aperture size.

SXFM measurement was performed with a test object using the apodized illumination and a distinct indication of improvement in the resolution has been observed. The effect of apodization has also been observed in the diffraction patterns of the non-

isolated object. An improvement in the visibility of the fringe in the diffraction pattern with apodized illumination has been observed. We have also presented the coherent x-ray diffractive imaging of a non-isolated object in a non-scanning mode.

In SXFM and CDI experiments, we realized different focal spot sizes at a fixed sample position by using a two-stage deformable KB mirror system. In this way, a unique feature of the optical system to generate variable focal spot size at a fixed focal point has been demonstrated. We expect that the optical system discussed here will find wide applications in various spectroscopic and microscopic techniques operated at the synchrotron light sources. The use of apodized illumination in SXFM can be extended to the biologically important specimens. Apodized-illumination CDI of non-isolated objects can be usefully applied to various samples of material and biological importance with synchrotron x-rays [19, 20] and x-ray free-electron lasers [21, 22].

References

- [1] A. Sakdinawat and D. Attwood, *Nat. Photon.* **4**, 840 (2010).
- [2] G. E. Ice et al., *Science* **334**, 1234 (2011).
- [3] C. J. Fahmi, *Curr. Opin. Struct. Biol.* **11**, 121 (2007).
- [4] M. D. de Jonge and S. Vogt, *Curr. Opin. Struct. Biol.* **20**, 606 (2010).
- [5] U. E. A. Fittschen and G. Falkenberg, *Spectrochim. Acta B* **66**, 567 (2011).
- [6] S. Majumdar et al., *Anal. Chim Acta* **755**, 1 (2012).
- [7] S. Matsuyama et al., *X-Ray Spectrom.* **39**, 260 (2010).
- [8] J. Miao et al., *Nature* **400**, 342 (1999).
- [9] I. Robinson and R. Harder, *Nat. Mater.* **8**, 291 (2009).
- [10] J. Miao et al., *Science* **348**, 530 (2015).
- [11] C. G. Schroer et al., *Phys. Rev. Lett.* **101**, 090801 (2008).
- [12] Y. Takahashi et al., *Phys. Rev. B* **80**, 054103 (2009).
- [13] T. Kimura et al., *Opt. Express* **21**, 9267 (2013).
- [14] K. Tamasaku et al., *Nucl. Instrum. Methods A* **467-468**, 686 (2001).
- [15] T. Kimura et al., *Jpn. J. Appl. Phys.* **48**, 072509 (2009).
- [16] P. Kirkpatrick and A. V. Baez, *J. Opt. Soc. Am.* **38**, 766 (1948).
- [17] Y. Suzuki et al., *Jpn. J. Appl. Phys.* **44**, 1994 (2005).
- [18] S. Marchesini et al., *Phys. Rev. B* **68**, 140101 (2003).
- [19] J. Miao et al., *Proc. Natl. Acad. Sci. U.S.A.* **100**, 110 (2003).
- [20] Y. Nishino et al., *Phys. Rev. Lett.* **102**, 018101 (2009).
- [21] M. M. Seibert et al., *Nature* **470**, 78 (2011).
- [22] T. Kimura et al., *Nat. Commun.* **5**, 3052, (2014).

Chapter VI. Conclusions and Future Prospects

This thesis, has introduced a new modality of coherent diffraction microscopy which can image non-isolate objects in a non-scanning mode. Experiments at optical and x-ray wavelengths have been discussed in order to establish the possibility of the proposed method.

In the process of experimental realization of the method, a specially designed experimental setup has been developed at both the spectral range. Employing the setup, generation of apodized illumination, imaging of non-isolated objects has been accomplished.

The experiments at the optical wavelength can be extended to obtain the refractive index maps of the cells and tissues. The non-scanning nature of the method would be suitable to image the dynamics of the bio-medically important specimens.

At x-ray wavelength, the current works can be improved and extended to the samples of importance in material and biological science. Suppressing the side lobes in the focused illumination to the values closer to the theoretical limits may improve the performance of the proposed method. In order to extract the utmost potential of the experimental system developed, current works can be extended to operate in multimodal configuration generating the fluorescence contrast and the diffraction contrast simultaneously. Similarly, the variable spot size at the sample plane can be fully utilized by extending the current works to lens-less microscopy with zoom function.

Acknowledgement

There are many people whom I owe a lot, who have helped me constantly during the tenure of my Phd studies. I thank all of them from the bottom of my heart. This list of people begins from my thesis supervisor Prof. Yoshinori Nishino whom I would like to thank for teaching me the technical aspects of the scientific research. I also thank him for creating a very interactive scientific environment in his group.

I would like to express my sincere gratitude to Dr. Takashi Kimura, who have been with me from the beginning of my days in coherent x-ray optics laboratory and have constantly supported in almost all the experimental works present in this thesis.

Thanks are also due to Prof. Kazuto Yamauchi for providing an opportunity to work with his world-class x-ray mirror system. I would also like to thank Dr. Satoshi Matsuyama, Dr. Hiroki Nakamori and Takumi Goto from the laboratory of Prof. Yamauchi for their endless help during the experiment at Spring-8.

I acknowledge the technical support from Dr. Yoshiki Kohmura during the experiments at Spring-8.

The entire administrative burdens during these four and half years of my stay in coherent x-ray optics laboratory have been taken by three different secretaries. Thank you very much Tagashira-san, Yuki-san and Yamazaki- san.

I would like to thank all the past and present members of coherent x-ray optics laboratory for their assistance in my personal and laboratory life.